AGU PUBLICATIONS

JGR

Journal of Geophysical Research: Planets

RESEARCH ARTICLE
10.1002/2016JE005248

Special Section:
Investigations of the Bagnold Dune Field, Gale crater

Key Points:
- We design and implement a Markov Chain Monte Carlo approach to spectral unmixing to test accuracies of the Hapke radiative transfer model
- Errors/uncertainties in abundances/grain sizes are quantified for two sets of laboratory ternary mixtures, with and without noise
- Large uncertainties due to nonunique fits highlight the usefulness of probabilistic approaches to spectral unmixing of remote sensing data

Correspondence to:
M. G. A. Lapotre,
mlapotre@caltech.edu

Citation:
Lapotre, M. G. A., B. L. Ehlmann, and S. E. Minson (2017), A probabilistic approach to remote compositional analysis of planetary surfaces, *J. Geophys. Res. Planets*, *122*, 983–1009, doi:10.1002/2016JE005248.

Received 20 DEC 2016
Accepted 5 APR 2017
Accepted article online 14 APR 2017
Published online 26 MAY 2017

A probabilistic approach to remote compositional analysis of planetary surfaces

M. G. A. Lapotre[1], B. L. Ehlmann[1,2], and S. E. Minson[3]

[1]Division of Geological and Planetary Sciences, California Institute of Technology, Pasadena, California, USA, [2]Jet Propulsion Laboratory, California Institute of Technology, Pasadena, California, USA, [3]U.S. Geological Survey, Earthquake Science Center, Menlo Park, California, USA

Abstract Reflected light from planetary surfaces provides information, including mineral/ice compositions and grain sizes, by study of albedo and absorption features as a function of wavelength. However, deconvolving the compositional signal in spectra is complicated by the nonuniqueness of the inverse problem. Trade-offs between mineral abundances and grain sizes in setting reflectance, instrument noise, and systematic errors in the forward model are potential sources of uncertainty, which are often unquantified. Here we adopt a Bayesian implementation of the Hapke model to determine sets of acceptable-fit mineral assemblages, as opposed to single best fit solutions. We quantify errors and uncertainties in mineral abundances and grain sizes that arise from instrument noise, compositional end members, optical constants, and systematic forward model errors for two suites of ternary mixtures (olivine-enstatite-anorthite and olivine-nontronite-basaltic glass) in a series of six experiments in the visible-shortwave infrared (VSWIR) wavelength range. We show that grain sizes are generally poorly constrained from VSWIR spectroscopy. Abundance and grain size trade-offs lead to typical abundance errors of $\leq$1 wt % (occasionally up to ~5 wt %), while ~3% noise in the data increases errors by up to ~2 wt %. Systematic errors further increase inaccuracies by a factor of 4. Finally, phases with low spectral contrast or inaccurate optical constants can further increase errors. Overall, typical errors in abundance are $<$10%, but sometimes significantly increase for specific mixtures, prone to abundance/grain-size trade-offs that lead to high unmixing uncertainties. These results highlight the need for probabilistic approaches to remote determination of planetary surface composition.

1. Introduction

In the past few decades, multispectral and hyperspectral data sets covering the ultraviolet-to-thermal-infrared wavelength ranges have revolutionized our understanding of the surface composition of many planetary bodies. Reflectance spectra allow the detection of key mineral and ice phases, and, when combined with quantitative semiempirical theories [e.g., *Hapke*, 1981; *Hapke and Wells*, 1981; *Hapke*, 1984, 1986; *Shkuratov et al.*, 1999; *Hapke*, 2002, 2008], enable the estimation of the composition and grain sizes of particulate surfaces ("spectral unmixing"). These models have been tested and used to invert for mineral abundances for laboratory particulate mixtures [e.g., *Clark and Roush*, 1984; *Mustard and Pieters*, 1987, 1989; *Hiroi and Pieters*, 1994; *Lucey*, 1998; *Poulet and Erard*, 2004; *Robertson et al.*, 2016] and for planetary surfaces from telescopic and orbiter-based spectroscopic data [e.g., *McCord et al.*, 1998; *Cruikshank et al.*, 2003; *Poulet et al.*, 2008; *Tirsch et al.*, 2011; *Poulet et al.*, 2014; *Edwards and Ehlmann*, 2015; *Goudge et al.*, 2015; *Liu et al.*, 2016; *De Sanctis et al.*, 2016].

In the vast majority of published mineral abundance retrievals, modeled mineral compositions have been found by searching for a best fit to a given spectrum by way of an optimization routine (e.g., using least squares with a grid search and a downhill simplex), and thus only provide single sets of mineral abundances, and sometimes grain sizes, that fit the data. However, the combined effects of mineral abundances, grain sizes, noise, and the nonlinearity of radiative transfer models lead to an ill-posed inverse problem; in particular, several equally good solutions may fit the data. For example, Figure 1 shows the laboratory spectrum of a 16 wt % olivine-16 wt % pyroxene-68 wt % plagioclase particulate intimate mixture (red) and two modeled spectra (green and blue), which both fit the data equally well (same RMS error) and yet correspond to significantly different modal mineralogies. In this particular case, nonuniqueness arises from trade-offs between mineral abundances and grain sizes (e.g., see olivine abundances and grain sizes in models 1 and 2; see also Figure 2b). Thus, a significant knowledge gap in visible-shortwave infrared (VSWIR) spectroscopy is that of the

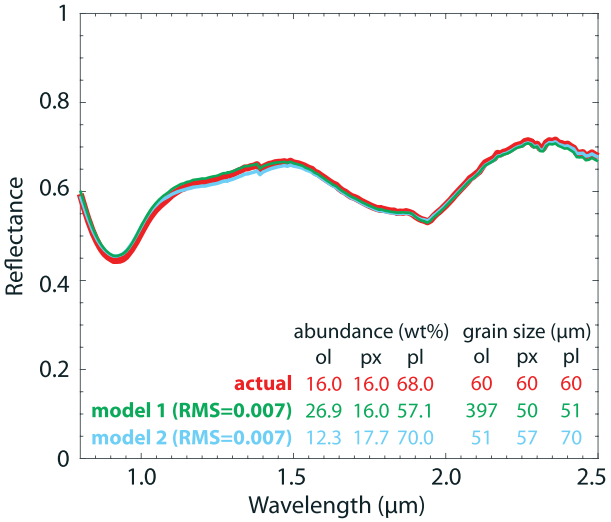

Figure 1. Example of two different synthetic mixtures fitting a laboratory spectrum equally well, as evaluated by computation of root-mean-square error in fit. The red spectrum is radiance coefficient as measured in the laboratory from a particulate mixture (~45–75 μm) of 16 wt % olivine ("ol")-16 wt % pyroxene ("px")- 68 wt % plagioclase ("pl") from *Mustard and Pieters* [1989] (see Table 1 for reference to spectral library). The green and blue spectra are modeled from the optical constants of olivine, pyroxene, and plagioclase by using the Hapke forward model. Both models correspond to very different modal compositions and yet have the same RMS error of 0.007.

quantitative errors and uncertainties associated with the inverse determination of mineral abundances and grain sizes. Constraining these would represent a major improvement to commonly used inversion techniques by shedding light onto the reliability of inferred compositions of planetary surfaces, i.e., by providing best fit estimates with rigorously understood uncertainties.

In this paper, we use a Bayesian approach, namely, a Markov chain Monte Carlo (MCMC) implementation [*Minson et al.*, 2013] of the Hapke scattering model [*Hapke*, 1981], to illustrate and quantitatively constrain the errors and uncertainties associated with spectral unmixing. We first summarize the inversion workflow, then describe the adopted forward model and Bayesian probabilistic approach. Finally, we illustrate the technique with six computational experiments that were designed to separately quantify the effects of inherently nonunique fits, noise, and specific spectral properties of the endmembers on errors and uncertainties by using both simulated and laboratory ternary mixtures (olivine-enstatite-anorthite and olivine-nontronite-basaltic glass). A seventh experiment, where we compare Mars orbiter-based data with ground truth, is the subject of a companion paper [*Lapotre et al.*, 2017].

2. Methods

In this section, we summarize the recommended workflow for probabilistic spectral unmixing, from the identification of mineral endmembers and calculation of their optical constants, to the forward model we use, and to the MCMC procedure. While we illustrate our approach with the Hapke radiative transfer model [*Hapke*, 1981], this general workflow can be employed regardless of the choice of the forward model details.

2.1. Workflow Overview

As light from an emitting source, e.g., the Sun, is reflected by a geologic surface, its spectrum becomes the carrier of useful compositional information. In particular, the ratio of received-to-incident light spectral flux is a complex convolution of how light interacted with any atmosphere as it traveled to and away from the geologic surface, of how it interacted with individual mineral/mineraloid/ice/organic crystals or grains on the surface, and of illumination geometry. For planetary remote sensing data, the instrument response also modulates the spectral information content of collected light. In this study, we only consider laboratory spectra from light that has not significantly interacted with the atmosphere and with highly stable instruments. Spectral interpretation is thus simplified to (i) knowing the illumination geometry, (ii) having a forward model to predict how mixtures of different mineral grains interact with light, and (iii) inverting for compositional information from the data using the forward model.

The reflectance of a mixture of mineral/mineraloid/icy/organic components is a function of the reflectances of those individual components. Thus, in order to perform spectral unmixing, one first needs to identify what components (all grouped under "mineral endmembers" herein) are present in the target. This identification is complex, and yet critical to the unmixing procedure, as it governs the inputs to the overall algorithm.

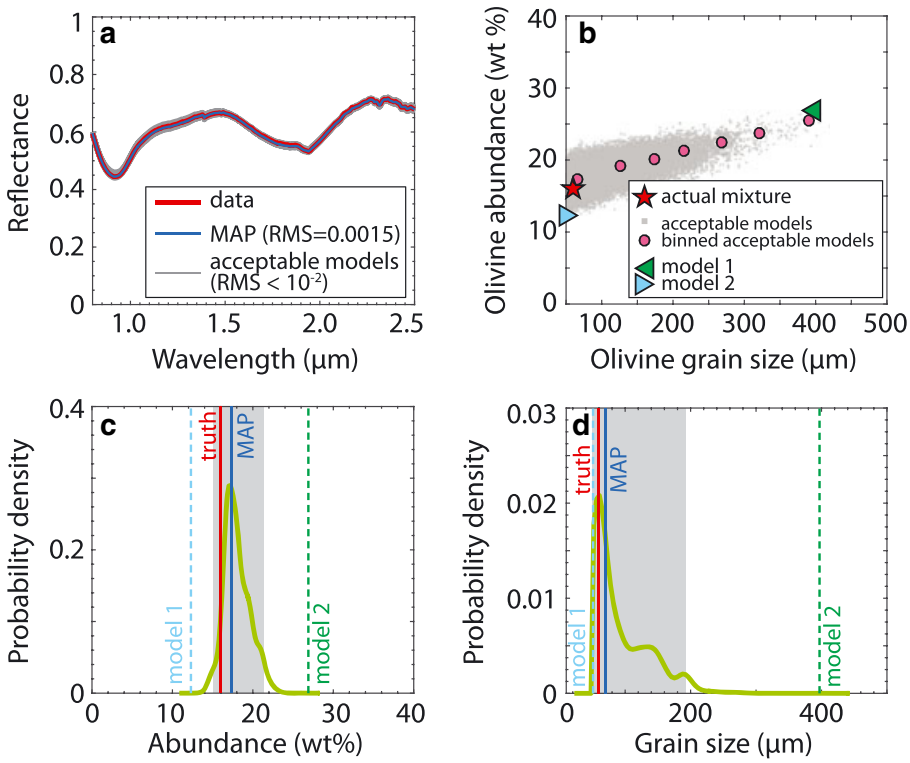

Figure 2. (a) Example of the maximum a posteriori probability model (MAP; blue) for the same mixture as in Figure 1 and set of "acceptable" models (RMS error $< 10^{-2}$; gray). (b) Correlation between the abundances and grain sizes of olivine that yield acceptable fits to the data (raw model data in gray dots, data binned by mean value over 50 μm size intervals in pink circles; RMS error between 0.0015 and 0.0099). Abundances and sizes corresponding to the actual mixture and models 1 and 2 from Figure 1 are denoted by a red star and green and blue triangles, respectively. Probability density of olivine (c) abundance and (d) grain size as determined from all acceptable models. True and MAP abundances and sizes are indicated by red and blue vertical solid lines, respectively. The vertical dashed lines correspond to the two models shown in Figure 1 (model 1 in light blue and model 2 in dark green). The shaded areas correspond to the 95% confidence intervals in olivine abundance and sizes. Note that while the MAP does not coincide with the truth, true abundance and grain size are both accepted with a high probability, emphasizing the usefulness of this probabilistic approach.

Identifying what mineral endmembers are appropriate to model spectral data may require an iterative procedure (section 2.2.1).

Nash and Conel [1974] showed that the VSWIR reflectance of an intimate mixture of grains is not a linear combination of the reflectances of its constitutive mineral endmembers due to multiple scattering of photons. *Hapke* [1981] developed a radiative transfer model that relates the reflectance of a mixture to a linear combination of the single-scattering albedos of its constituent endmembers. Because the single-scattering albedo of a single mineral is a function of its optical constants (real and imaginary indices of refraction, n and k, respectively) and grain size, spectral unmixing requires the measurement or computation of the optical constants of all mineral endmembers as a function of wavelength. In the absence of available transmission spectra, optical constants need be determined from laboratory spectra by using a radiative transfer model (section 2.2.3). The Hapke formulation has the advantage that single-scattering albedos do mix linearly with mixing coefficients relating grain size and density (section 2.3). Thus, with the mineral endmembers' optical constants on hand to calculate single-scattering albedos, one can invert for the composition and grain sizes of a particulate mixture by minimizing the mismatch between computed mixture spectra and the data.

The goodness of a given forward model may be evaluated by calculating the root-mean-square (RMS) error between the data and the forward model and minimizing it, e.g., through a brute-force grid search over all parameters or, e.g., a downhill simplex [e.g., *Poulet and Erard*, 2004; *Ehlmann*, 2010]. However, due to the nonuniqueness of the solution (due to, e.g., abundance and grain size trade-offs and/or noise) and systematic error from the forward model (which affect both optical constants inverted from reflectance spectra and

modeled particulate mixtures), we adopt the approach of finding a range of solutions that reasonably match the data (e.g., Figures 2a and 2b). To do so, we use a MCMC approach (section 2.4) which allows sampling the parameter space at a density that is proportional to the likelihood of a given model, which itself is a function of the goodness of the fit (RMS error) between a given forward model and the data.

The outputs of the MCMC algorithm are the probability densities of mineral abundances (e.g., Figure 2c) and grain sizes (e.g., Figure 2d). Several useful descriptors may be evaluated from the probability density functions (PDFs), such as (i) the maximum a posteriori probability model (or MAP), which corresponds to the most sampled area of the parameter space, i.e., the most probable mineral assemblage, and (ii) the 95% confidence interval of a given parameter, which is a measure of uncertainty (e.g., Figures 2c and 2d). Note that the 95% confidence interval would correspond to $\pm 2\sigma$ (standard deviation) if the PDFs were Gaussian. The difference between the truth and the MAP is a measure of error, while the width of the 95% confidence interval is a measure of uncertainty (Figure 2). Figure 2a shows the same laboratory spectrum as in Figure 1 (red), along with its corresponding MAP spectrum (blue) and example models that one could deem acceptable (gray), especially if the data were noisy. The PDFs of mineral assemblages are built from the mineral abundances (e.g., Figure 2c) and grain sizes (Figure 2d) corresponding to those spectra that are deemed acceptable. The MCMC-determined probability density allows the likelihood of any given mineral assemblage to be assessed quantitatively.

2.2. Mineral Endmember Identification and Optical Constants

2.2.1. Endmember Identification

Different approaches in selecting mineral endmembers have been used for different wavelength ranges, from a simple visual inspection of spectra for VSWIR data [e.g., *Poulet et al.*, 2014] to a search over a large spectral library for thermal-infrared spectra [*Feely and Christensen*, 1999]. Statistical methods can also be used to find in-scene endmembers from hyperspectral data cubes [e.g., *Tompkins et al.*, 1997; *Thomas and Bandfield*, 2013]. An additional complication comes from the presence of phases that do not have distinctive absorption features that impart characteristic spectral signatures, e.g., iron-free plagioclases in the VSWIR or halides in the MIR. While increasing the number of mineral endmembers used to perform an inversion typically improves the goodness of the fit, it is unclear whether such an improvement has any physical meaning, i.e., whether constituents modeled at small abundances are actually present.

As an overall approach for VSWIR spectral unmixing, we suggest that mineral endmembers should be selected parsimoniously on the basis of (1) required mineral phases, uniquely identifiable from distinct absorptions in the data (e.g., broad absorptions near 1 μm and 2 μm signal the presence of pyroxenes or basaltic glasses and characteristic sharp absorptions of –OH and H_2O at ~1.4, ~1.9, and ~2.3 μm require the presence of Fe/Mg phyllosilicates), (2) geologic context (e.g., mafic rocks are likely to contain both VSWIR spectrally undistinctive plagioclase as well as pyroxenes), and (3) requirements for overall albedo (e.g., opaque phases, such as kerogens or iron oxides, selected based on context, may be required to match a spectrum's low albedo). If necessary, more mineral endmembers may be added iteratively.

Mafic mixtures are the focus of this study, as mafic protoliths are common on many planetary surfaces. Common minerals (and absorptions) that may be present in mafic mineral assemblages include olivine (broad 1 μm feature, with a shape that changes depending on Fe content [e.g., *Sunshine and Pieters*, 1998]), pyroxenes (broad 1 μm and 2 μm absorptions, with positions that shift depending on Fe and Ca content [e.g., *Klima et al.*, 2011, and references therein]), plagioclases (which have a 1.3 μm feature for Fe-bearing phases but are otherwise featureless in the VSWIR [e.g., *Cheek and Pieters*, 2014]), and iron oxides (which have electronic absorptions at <1 μm but are often featureless in the SWIR ([e.g., *Burns*, 1993; *Morris et al.*, 1993]). Clinopyroxenes and orthopyroxenes may both be present depending on the source composition, temperature, and degree of partial melting. Thus, for mafic compositions in the VSWIR wavelength range, we implement the overall endmember selection approach above as follows:

1. Examine the spectral properties near 1 μm to determine if the shape and breadth of the observed 1 μm feature require olivine to be present.
2. If olivine appears to be present, pick a single pyroxene that best matches the ~2 μm absorption, if present.
3. Add any other phases required by observed absorption features present (e.g., nontronite, saponite, chlorite, or other mafic alteration products).

4. Assume the presence of plagioclase and an Fe oxide (inspect the visible spectral range to determine which Fe oxide); those two phases generally trade-off with each other and with phases with absorptions in setting the overall SWIR albedo.
5. Iterate and visually inspect fit width near 1 μm to identify the olivine composition (Fo number).
6. Inspect the residuals for remaining pyroxene signatures and add a second pyroxene if it is required to match the width of the ~2 μm absorption.
7. Other phases may be added from inspection of the remaining residuals or context (e.g., amorphous glass, other Fe oxides, and additional hydrated phases).

Once mineral endmembers are identified by using iterative modeling and the qualitative steps described above, their respective densities and optical constants are used as inputs to our quantitative algorithm.

The reflectance or emission of an endmember constituent is a function of its density, grain size, and optical constants. In the MIR for coarse-grained samples, the values of the optical constants are such that photons are mostly singly scattered and reflectance or emission spectra acquired in the laboratory can be directly used in modeling (see *Clark* [1999] for review). For fine-grained constituents in the MIR (< ~60 μm [e.g., *Ramsey and Christensen*, 1998]) or all grain sizes in the VSWIR, multiple scattering causes grain size to exert a key control on spectral properties. In this case, endmember optical constants must be employed rather than reflectance or emission spectra.

2.2.2. Conversion of Reflectance to Single-Scattering Albedo

Optical constants can be derived directly from laboratory measurement of crystalline minerals in transmission [e.g., *Zeidler et al.*, 2011] or estimated from laboratory reflectance spectra of a particulate sample via conversion of its reflectance to its single-scattering albedo [*Roush et al.*, 1990; *Lucey*, 1998; *Roush*, 2003]. Single-scattering albedo is a dimensionless measure of the proportion of light scattered by a grain in a single interaction, expressed as a function of wavelength. For a geometric optics regime (when particles are larger than a few wavelengths of light), *Hapke* [1981] proposed that single-scattering albedo, w, and reflectance (precisely, the radiance coefficient), r, are related through

$$r(\mu,\mu_0,\mathrm{g}) = \frac{w}{4(\mu+\mu_0)}\left[(1+B(g))P(g) + H(w,\mu)H(w,\mu_0) - 1\right] \tag{1a}$$

where μ_0 is the cosine of the incidence angle, μ is the cosine of the emergence angle, g is the phase angle, B is the backscattering function, and P is the phase function of the material. The H function is the Chandrasekhar integral function associated with the observation geometry. For the laboratory spectra considered here, we assume $B = 0$ (no backscattering at the moderate phase angles measured) and $P = 1$ (isotropic scatterers), i.e.,

$$r(\mu,\mu_0) \approx \frac{w}{4(\mu+\mu_0)} H(\mu)H(\mu_0). \tag{1b}$$

Mustard and Pieters [1989] showed that when grain sizes are known and a more realistic formulation of the photometric phase function is used, inverted abundances can typically be improved by a few weight percent.

Following *Hapke* [2002], we approximate the Chandrasekhar function by

$$H(\mathrm{x}) \approx \frac{1}{1 - wx\left[r_0 + \frac{(1-2r_0x)}{2}\ln\left(\frac{1+x}{x}\right)\right]}, \tag{2}$$

where $r_0 = \frac{1-\gamma}{1+\gamma}$ is the bihemispherical reflectance for isotropic scatterers, $\gamma = \sqrt{1-w}$, and x is used as a generic input variable.

Inverting for w in equation (1b) yields the approximate expression we use for the single-scattering albedo,

$$w \approx \frac{4(\mu+\mu_0)r}{H(\mu)H(\mu_0)}, \tag{3}$$

where H is calculated from equation (2).

Because equation (1) applies to both the reflectance of a particulate mixture and its individual constituents, one can use the measured reflectance of a pure particulate sample to invert for the single-scattering albedo of its constitutive grains. In order to disentangle the effects of composition and grain size on single-scattering albedo of mineral endmembers, we now need to express w as a function of the component's optical constants, n and k, and grain diameter, D.

2.2.3. Conversion of Single-Scattering Albedo to Imaginary Index of Refraction

Following *Hapke* [1981], the single-scattering albedo of a particulate sample can be expressed as

$$w = S_e + (1 - S_e)\frac{(1 - S_i)}{1 - S_i\Theta}\Theta, \tag{4}$$

where

$$S_e = \frac{(n-1)^2 + k^2}{(n+1)^2 + k^2} + 0.05 \tag{5}$$

is the surface reflection coefficient for externally incident light,

$$S_i = 1.014 - \frac{4}{n(n+1)^2} \tag{6}$$

is the reflection coefficient for internally scattered light [*Lucey*, 1998], and

$$\Theta = \frac{r_i + \exp\left(-\sqrt{\alpha(\alpha+s)}\langle D\rangle\right)}{1 + r_i \exp\left(-\sqrt{\alpha(\alpha+s)}\langle D\rangle\right)} \tag{7}$$

is the particle internal transmission coefficient, and where r_i is the internal diffusive bihemispherical reflectance inside a particle, α is the internal absorption coefficient, s is the internal scattering coefficient, and $\langle D\rangle$ is the mean free path of a photon.

The internal bihemispherical reflectance in a particle can be expressed as

$$r_i = \frac{1 - \sqrt{\frac{\alpha}{\alpha+s}}}{1 + \sqrt{\frac{\alpha}{\alpha+s}}}, \tag{8}$$

where

$$\alpha = \frac{4\pi k}{\lambda}. \tag{9}$$

is the internal absorption coefficient, with λ, the wavelength of light. We assume $s = 0$, following the reasoning of *Lucey* [1998] for natural particles. Finally, the mean free path $\langle D\rangle$ is estimated from D and n through

$$\langle D\rangle = \frac{2}{3}\left[n^2 - \frac{1}{n}\left(n^2 - 1\right)^{\frac{3}{2}}\right]D. \tag{10}$$

For typical n values ($n \sim 1.5$–2.5), $\langle D\rangle \approx 0.9D$, in keeping with the formulation of *Lucey* [1998].

Combining equations (3)–(10) and measurements of pure particulate spectra of known grain sizes, one can solve for the imaginary index of refraction, k, by finding the value of k that minimizes the misfit between the corresponding calculated w (equations (4)–(10)) and the single-scattering albedos of the sample (equation (3)) at each wavelength with an assumed n and D. While there are sophisticated models to calculate both optical constants (n and k) simultaneously (e.g., Kramers-Kronig dispersion theory [*Kronig*, 1926; *Kramers*, 1927]), the real index of refraction, n, does not typically vary by more than ~0.1 within the wavelength range we consider (~0.8–2.5 μm), and we treat it as a constant [e.g., *Roush et al.*, 1990; *Lucey*, 1998; *Roush*, 2003]. Reductions on uncertainties with variable n were explored and found to be unimportant. Ideally, the inversion is performed iteratively for samples of different grain sizes to minimize the uncertainty associated with the effective grain size of a given laboratory sample. Errors of up to 10–15% in endmember reflectance may arise if optical constants are not optimized [e.g., *Lucey*, 1998; *Poulet and Erard*, 2004].

Now that we can calculate the single-scattering albedo of a particulate mixture, w_{mix}, from its reflectance spectrum, and the single-scattering albedo of individual endmembers, w_i, from grain size and optical constants, we need to relate w_{mix} to the w_i of its constitutive endmembers.

2.3. Forward Modeling of Mixture Spectra From Mineral Endmembers

While there exist several models to predict the VSWIR spectrum of a particulate mixture from spectra of its individual components [e.g., *Purcell and Pennypacker*, 1973; *Hapke*, 1981; *Shkuratov et al.*, 1999], there is no model that consistently yields better results than the others, and the uncertainties associated with them

appear to remain large [e.g., *Poulet et al.*, 2002]. To illustrate the usefulness of our Bayesian approach to VSWIR spectroscopy, we use the widely employed Hapke model [*Hapke*, 1981].

Because the reflectance of a mixture is a nonlinear function of the reflectances of its individual mineral components, a first step is to convert reflectance to a quantity that does mix linearly—the single-scattering albedo. The single-scattering albedo of a mixture of grains, w_{mix}, is a linear combination of the single-scattering albedos of its individual endmembers, w_i, such that

$$w_{\mathrm{mix}} = \sum_{i=1}^{N} f_i w_i, \tag{11}$$

where f_i is the fractional relative cross section of component i and is given by

$$f_i = \frac{\sigma_i}{\sum_{i=1}^{N} \sigma_i}, \tag{12a}$$

where

$$\sigma_i = \frac{m_i}{\rho_i D_i} \tag{12b}$$

and m_i is the mass abundance, ρ_i is the density, and D_i is the grain size of endmember i. Note that equation (12) is mathematically equivalent to the original formulation of Hapke [*Hapke*, 1981], in which f_i is written in terms of bulk density of mineral i, i.e., the combined mass of particles of mineral i per unit total volume (including void space and other mineral grains). Indeed, in Hapke's formulation, the total-volume terms, which do not vary with index i, cancel out; similarly, when using equation (12) and thus mass abundance (i.e., the combined mass of particles of mineral i per total unit mass of the particulate mixture), the total-mass term does not vary with index i, such that they cancel out when taking the ratio of σ_i to $\sum_{i=1}^{N} \sigma_i$.

The misfit between actual single-scattering albedo of a mixture and modeled mixture single-scattering albedos is then minimized to invert for mineral abundances (m_i) and grain sizes (D_i). However, as the solution to this inverse problem can be nonunique (e.g., Figure 1), we adopt a Bayesian approach to constrain likely mineral assemblages.

2.4. Inverse Model: Bayesian Inversion of Mineral Abundances and Grain Sizes

Traditional optimization methods for solving the unmixing inverse problem identify one possible set of values for grain sizes and mineral abundances. However, we know that there is considerable uncertainty in inverted mineral composition because multiple mineral assemblages are compatible with the observations (e.g., Figures 1 and 2). Thus, instead of using an optimization approach, we adopt a Bayesian inversion approach (section 2.4.1) that allows us to determine the ensemble of all plausible composition models (mineral abundances and grain sizes) that are consistent with both the observations (e.g., Figure 2) and our a priori knowledge of likely grain sizes and mineral abundances (section 2.4.2). Another advantage of Bayesian methods is that we can account for both errors in our measurements (e.g., instrument noise) and errors and uncertainties associated with our physical model for mapping mineral composition into spectral observations (e.g., model inputs, reflectance model physical parameterization, and atmospheric correction). In the next section, we explore how we build the Bayesian posterior probability density function (PDF), i.e., the PDF that describes the relative probability of different values for mineral abundances and grain sizes given our observations and a priori information.

Unfortunately, except for certain special cases, Bayesian posterior PDFs generally do not have a simple analytical form. Thus, to explore the posterior PDF, we must simulate it by using a Markov chain Monte Carlo (MCMC) algorithm to draw a large ensemble of random samples of the posterior PDF. From these samples, we can then estimate any statistics of interest on the mineral assemblage (e.g., mean, median, and confidence intervals). In the following sections, we describe our sampling methodology.

2.4.1. Principles of Bayesian Inference

Our goal is to infer the PDF that describes the relative plausibility of all potential mineral abundances and grain sizes, given our observations. Mathematically, we write this as $p(\mathbf{m}, \mathbf{D} | \mathbf{d})$, i.e., the probability density

for different values for our mineral abundances, **m**, and grain sizes, **D**, given our observed wavelengths and single-scattering albedo data values, **d**. For our problem, **d** is a vector containing the spectral data (of length $2N_d$, containing N_d wavelengths and N_d corresponding single-scattering albedo values), and **m** and **D** are vectors of the values of the mineral abundances and grain sizes that we are trying to assess, each with a length equivalent to the number of components, N.

Bayes' theorem [*Bayes*, 1763] states that the posterior PDF, i.e., the probability of a set of model parameters, **m** and **D**, given the observations, **d**, is

$$p(\mathbf{m},\mathbf{D}|\mathbf{d}) \propto p(\mathbf{d}|\mathbf{m},\mathbf{D})p(\mathbf{m},\mathbf{D}), \tag{13}$$

where $p(\mathbf{m},\mathbf{D}) = p(\mathbf{m})p(\mathbf{D})$ is the prior PDF that defines the a priori relative probability of different values of the mineral abundances and grain sizes before making any spectral observations. We describe how we represent our a priori knowledge of mineral abundances and grain sizes in section 2.4.2. The other term in the posterior PDF (equation (13)) is the data likelihood, $p(\mathbf{d}|\,\mathbf{m},\mathbf{D})$. Data likelihood is the PDF that describes the probability of having observed the spectral data, **d**, given a particular set of values for **m** and **D**. If we assume Gaussian errors, then the data likelihood function is a normal distribution.

In detail, let $\boldsymbol{\delta}$ be the measurement predictions corresponding to the data, **d**, and $G(\mathbf{m},\mathbf{D})$ a function describing the deterministic forward model (i.e., Hapke's model in our case; section 2.3), such that

$$\boldsymbol{\delta} = G(\mathbf{m},\mathbf{D}) + \mathbf{e} + \boldsymbol{\varepsilon}, \tag{14}$$

where **e** is the uncertainty due to measurement errors (e.g., associated with the noise in spectral data) and $\boldsymbol{\varepsilon}$ is the uncertainty due to model prediction errors (e.g., associated with inaccurate predictions by $G(\mathbf{m},\mathbf{D})$, i.e., the physics in the model). We assume that measurement and prediction errors (each of length $2N_d$), **e** and $\boldsymbol{\varepsilon}$, can be modeled by independent Gaussian PDFs, such that the likelihood function $p(\mathbf{d}|\,\mathbf{m},\mathbf{D})$ is given by

$$p(\mathbf{d}|\mathbf{m},\mathbf{D}) = \frac{1}{(2\pi)^{N_d}\left|\mathbf{C}_\chi\right|^{\frac{1}{2}}} \exp\left\{-\frac{1}{2}[\mathbf{d} - G(\mathbf{m},\mathbf{D}) - \boldsymbol{\eta}]^{\mathrm{T}}\mathbf{C}_\chi[\mathbf{d} - G(\mathbf{m},\mathbf{D}) - \boldsymbol{\eta}]\right\}, \tag{15}$$

where $\mathbf{C}_\chi$ and $\boldsymbol{\eta}$ are the covariance matrix and mean of the sum $(\mathbf{e}+\boldsymbol{\varepsilon})$, respectively. By definition, $\mathbf{C}_\chi$ is square and of dimensions equal to the length of **d** (i.e., $2N_d \times 2N_d$). In our implementation of the algorithm, we assume $\boldsymbol{\eta} = 0$, i.e., we model the uncertainty in our predicted wavelengths and single-scattering albedo values with a Gaussian distribution. In other words, we do not expect there to be a consistent bias between our predictions and the observed data values. In this study, we assume that our covariance matrix is isotropic, i.e., that overall error is not a function of wavelength. This assumption can be improved in future implementations with a model for how systematic errors in the Hapke forward model and/or instrument noise vary with wavelength.

2.4.2. A Priori Distributions of Abundances and Grain Sizes

In this section, we describe how we incorporate a priori knowledge on mineral abundances and grain sizes. Specifically, we assume that all values of abundances are equally likely so long as the abundances of all component minerals sum to unity, and we use uniform probability distributions to describe the possible grain sizes with lower and upper bounds based on our knowledge of plausible sizes (e.g., in the case of real planetary surfaces, from thermal inertia, or presence of bedforms).

2.4.2.1. Prior Distribution of Abundances

A requirement for the prior distribution of component abundances is that they must sum up to unity. A Dirichlet distribution is the simplest distribution that satisfies this assumption, and we thus assume that the probability density of abundances (N endmembers) follows a Dirichlet distribution,

$$p(\mathbf{m}) = \mathrm{Dir}(m_1,\ldots,m_N;a_1,\ldots,a_N) = \frac{1}{\mathrm{B}(\mathbf{a})}\prod_{i=1}^{N} m_i^{a_i-1}. \tag{16}$$

with $0 \leq m_i \leq 1$ (abundance of mineral i) and $\sum_{i=1}^{N} m_i = 1$, and where a_i are the concentration parameters discussed below, and B is the multinomial beta function

$$\mathrm{B}(\mathbf{a}) = \frac{\prod_{i=1}^{N} \Gamma(a_i)}{\Gamma\left(\sum_{i=1}^{N} a_i\right)}, \tag{17}$$

where $\mathbf{a}$ is the vector $(a_1, \ldots, a_N)$ and Γ is the gamma function

$$\Gamma(a_i) = \int_0^{\infty} x^{a_i - 1} e^{-x} \mathrm{d}x. \tag{18}$$

For $a_i > 0$,

$$\Gamma(a_i) = (a_i - 1)!. \tag{19}$$

Each concentration parameter, a_i, is a measure of the evenness (uniformity) or sparseness (values concentrated in a single value or narrow range of values) of the individual endmember distribution. When $a_i = 1$ for all N concentration parameters, all sets of probability distributions are equally likely. When $\sum_{i=1}^{N} a_i \rightarrow \infty$ instead, only near-uniform individual distributions are likely, i.e., each individual endmember distribution is a one-dimensional near-uniform distribution. When $\sum_{i=1}^{N} a_i \rightarrow 0$, only distributions with nearly all of the mass being concentrated within one component are likely. We assume $a_i = 1$, such that all sets of probability distributions are equally likely a priori.

2.4.2.2. Prior Distribution of Grain Sizes

In the absence of prior information on grain sizes (or to simulate the lack thereof), we model the a priori grain size probability densities as uniform distributions

$$p(D_i) = U(D_i) = \begin{cases} \dfrac{1}{D_{i,\max} - D_{i,\min}}, \text{for } D_i \in \left[D_{i,\min}, D_{i,\max}\right] \\ 0, \text{otherwise} \end{cases}, \tag{20}$$

where $D_{i,\min}$ and $D_{i,\max}$ are modeler-defined lower and upper bounds on the grain size range of mineral endmember i, respectively. For example, such bounds may be estimated from contextual indicators on planetary surfaces, such as the presence/absence of bedforms or from independent photometric or thermal inertia data sets. We note that the prior distribution on grain size is an "initial guess" of the distribution of grain sizes that may explain the data reasonably well, and thus does not reflect the grain size distribution within the geologic target.

2.4.3. Metropolis Algorithm

Substituting equations (15)–(16) and (20) into the posterior PDF (equation (13)) forms the product of multivariate normal, Dirichlet, and uniform distributions, which has no simple analytical solution. We thus stochastically simulate the posterior PDF of the observations by using a MCMC algorithm to draw random sample models whose density is proportional to the posterior PDF. The most common MCMC method is the Metropolis algorithm [*Metropolis et al.*, 1953]. The Metropolis algorithm uses a random walk to propose possible samples of some arbitrary target PDF (in this case, our posterior PDF) and then probabilistically chooses to accept or reject each candidate sample based on its probability in the target PDF.

The candidate samples are drawn from some known probability distribution, typically chosen to be a normal distribution. If a candidate sample of random values for our mineral abundances and grain sizes has higher posterior probability than the last sample, it is always accepted. As a result, the sampler obtains samples in the high-probability region of the posterior PDF even if the candidate has a low probability in the normal distribution being used to generate candidate samples. If the candidate sample has lower posterior probability than the current sample, the algorithm chooses to accept or reject that sample based on whether its posterior probability is greater than a draw from a standard uniform distribution between 0 and 1. Thus, low-probability candidate samples are proportionally accepted less often than high-probability candidate samples, creating a population of accepted samples whose density is proportional to the target posterior PDF. However, low-probability samples are rarely accepted, assuring that given enough samples, the

random walk eventually leaves a high-probability region in which it is currently located, thus ultimately visiting all parts of the potentially multimodal probability distribution describing the relative plausibility of different mineral assemblages.

Mathematically, the Metropolis algorithm works as follows. For notational simplicity, let us describe the unknown values describing the mineral composition with a single variable, $\boldsymbol{\theta} = \langle \mathbf{m}^{\mathrm{T}}, \mathbf{D}^{\mathrm{T}} \rangle^{\mathrm{T}}$, a vector containing possible values of our mineral abundances, **m**, and grain sizes, **D**. The Metropolis algorithm generates sample models $\{\boldsymbol{\theta}_1, \boldsymbol{\theta}_2, \ldots, \boldsymbol{\theta}_L\}$ (where L is the length of the Markov chain) of the target PDF via a random walk: given a current sample, $\boldsymbol{\theta}_i$, a new candidate sample, **y**, is generated and then probabilistically either accepted or rejected as θ_{i+1}. Commonly, $\mathbf{y} = \boldsymbol{\theta}_i + \mathbf{z}$ where **z** is drawn from a zero-mean multivariate normal distribution with arbitrary covariance, $\boldsymbol{\Sigma}$. The criterion for accepting or rejecting a sample is

$$\begin{cases} \boldsymbol{\theta}_{i+1} = \mathbf{y} \text{ if } \phi \geq u, \\ \boldsymbol{\theta}_{i+1} = \boldsymbol{\theta}_i \text{ otherwise,} \end{cases} . \tag{21a}$$

with

$$\phi = \min\left\{1, \frac{p(\mathbf{d}|\mathbf{y})p(\mathbf{y})}{p(\mathbf{d}|\boldsymbol{\theta}_i)p(\boldsymbol{\theta}_i)}\right\} = \min\left\{1, \frac{p(\mathbf{d}|\mathbf{y})p(\mathbf{y})}{p(\mathbf{d}|\mathbf{m}_i, \mathbf{D}_i)p(\mathbf{m}_i, \mathbf{D}_i)}\right\}, \tag{21b}$$

and where u is drawn from the standard uniform distribution, $U(0, 1)$, for each candidate sample, and $p(\mathbf{d}|\,\mathbf{y})$ and $p(\mathbf{d}|\,\boldsymbol{\theta}_i)$ are calculated according to equation (15). A nontrivial consequence of this sampling strategy is that the parameter space is sampled with density proportional to the posterior PDF, $p(\mathbf{m}, \mathbf{D}|\,\mathbf{d}) \propto p(\mathbf{d}|\,\mathbf{m}, \mathbf{D})p(\mathbf{m}, \mathbf{D})$, even though candidate sample models are proposed from an arbitrary PDF, e.g., $\mathbf{z} \sim N(0, \boldsymbol{\Sigma})$ [e.g., *Chib and Greenberg*, 1995].

2.4.4. Specifics of Our Implementation of the Metropolis Algorithm: Cascading Adaptive Transitional Metropolis In Parallel

The efficiency of the Metropolis algorithm is limited by several factors. First, if the proposal PDF used to generate candidate samples is very different from the target PDF (which it typically is since we are blindly sampling a target PDF whose shape and features we do not know), very few of our proposed candidate samples are accepted. If the acceptance rate is low, then the random walk explores the posterior PDF very slowly, staying in one location while many candidate samples are proposed and rejected. Second, if the posterior PDF is narrowly peaked, it may take a long time for the random walk to find the high-probability region. Third, for multimodal posterior PDFs, it may take a long time for the random walk to move from one high-probability region to another. Thus, to increase MCMC sampling efficiency, we use the Cascading Adaptive Transitional Metropolis In Parallel (CATMIP) algorithm [*Minson et al.*, 2013; *Minson et al.*, 2014], an approach that addresses all of these three efficiency issues.

First, CATMIP uses transitional PDFs [*Beck and Au*, 2002; *Ching and Chen*, 2007]—instead of attempting to sample the posterior PDF directly, CATMIP simulates a sequence of transitional PDFs. The first of these transitional PDFs is the prior PDF, which we know and can sample directly by using a random number generator. We then use each of these samples as the seed for a Metropolis random walk whose target is a new transitional PDF that is similar to the prior but is slightly closer to the posterior PDF (note that only the last sample from each Markov chain is kept, keeping the total number of samples unchanged). Because this target PDF is, by construction, close to our prior distribution, it takes little sampling effort to redistribute our samples so that their density is proportional to the new target PDF. Once this is accomplished, we then evolve our target PDF slightly closer to the posterior PDF, run the sampling again until we have simulated this new target PDF, and repeat until we finally simulate the posterior PDF itself. By evolving from a set of samples that are distributed according to our relatively flat prior distribution to the potentially highly peaked posterior PDF, we take away from the Metropolis algorithm much of the work of locating the high-probability regions of the posterior PDF and distributing our samples with density proportional to the posterior probability.

Mathematically, we write our series of transitional PDFs as

$$p_j = p_j\left(\mathbf{m}, \mathbf{D}|\mathbf{d}, \beta_j\right) \propto p(\mathbf{d}|\mathbf{m}, \mathbf{D})^{\beta_j} p(\mathbf{m}, \mathbf{D}), \tag{22}$$

where $j = 0, 1, \ldots, J$, and $0 = \beta_0 < \beta_1 < \ldots < \beta_J = 1$, where J is the total number of transitional PDFs (dynamically defined by $\beta_J = 1$). At the initial step, $p_0(\mathbf{m}, \mathbf{D}|\,\mathbf{d}, \beta_0 = 0) \propto p(\mathbf{d}|\,\mathbf{m}, \mathbf{D})^0 p(\mathbf{m}, \mathbf{D}) = p(\mathbf{m}, \mathbf{D})$ can be simulated by drawing sample models directly from the prior PDF. For β_1 sufficiently small, $p_1(\mathbf{m}, \mathbf{D}|\,\mathbf{d}, \beta_1)$ is similar enough

to $p_0(\mathbf{m}, \mathbf{D}|\, \mathbf{d}, \beta_0 = 0)$ that little Monte Carlo simulation is required to update the sample models of p_0 to be distributed according to p_1. Specifically, each sample of p_0 is updated with an independent instance of the Metropolis algorithm. These instances can be run in parallel, greatly decreasing the time required to execute the Monte Carlo sampling. Each succeeding transitional PDF can be similarly efficiently sampled until $p_j(\mathbf{m}, \mathbf{D}|\, \mathbf{d}, \beta_j = 1) \propto p(\mathbf{d}|\, \mathbf{m}, \mathbf{D})^1 p(\mathbf{m}, \mathbf{D}) = p(\mathbf{d}|\, \mathbf{m}, \mathbf{D}) p(\mathbf{m}, \mathbf{D})$ has been sampled, thus simulating the posterior PDF. The values for β_j, which define the series of transitional PDFs, are chosen to optimize the trade-off between improving the ease of sampling each transitional PDF (by evolving β slowly and thus keeping the new transitional PDF close to the previous PDF) with minimizing the number of transitional PDFs that must be sampled before reaching the posterior PDF. To this end, each succeeding value for β_{j+1} is chosen dynamically following *Beck and Zuev* [2013] and *Minson et al.* [2013].

CATMIP features other dynamic adaptations to further increase sampling efficiency. First, after each update from β_j to β_{j+1}, we resample our sample models of p_j with probability proportional to $\frac{p_{j+1}}{p_j}$ so that sample models are distributed more similarly to p_{j+1} [*Ching and Chen*, 2007]. This allows samples to be instantly relocated from relatively lower probability regions to higher-probability regions, combatting all three inefficiencies of the Metropolis algorithm. Second, the efficiency of each instance of the Metropolis algorithm is improved by optimizing the proposal PDF. Specifically, we choose the covariance matrix of the proposal PDF, $\mathbf{\Sigma}$, for p_{j+1} to be the covariance of the sample models of p_j reweighted to account for the updated value of β_{j+1} and scaled according to the acceptance rate from sampling p_j. This way, CATMIP automatically adapts its random walk to the covariances of the target PDF and rescales its step size to take larger steps when the acceptance rate is high and smaller steps when the acceptance rate is low, reducing potential inefficiency of the Metropolis algorithm due to a low acceptance rate. For more details on CATMIP, see *Minson et al.* [2013].

3. Procedure Tests With Ternary-Mixture Experiments

3.1. Experimental Design and Assumptions

We test the accuracy and uncertainties of spectral unmixing, using the workflow and algorithms detailed above in a set of six experiments. In the first four experiments, we consider ternary mixtures of olivine, enstatite, and anorthite with endmembers sieved to 45–75 μm grain sizes (Figure 3a and Table 1). The fifth and sixth experiments explore ternary mixtures of olivine, nontronite, and basaltic glass, each sieved to 45–75 μm grain sizes (Figure 3b and Table 1). The latter mixtures are more challenging due to the presence of basaltic glass, which has a low spectral contrast in the VSWIR wavelength range.

In the first experiment, we explore only computational aspects by using synthetic (computed) spectra. We use optical constants inverted from the laboratory reflectance spectra of the mineral endmembers of *Mustard and Pieters* [1987, 1989] and generate a suite of synthetic mixture spectra of known compositions by using the forward Hapke model. We then attempt to unmix those same computed spectra back for composition and grain size. This experiment is designed to eliminate effects from any systematic error in the forward model. That is, we know that the forward model is able to exactly reproduce the mixture spectra because it was directly used to generate them. Thus, experiment 1 highlights any nonuniqueness in the solution that solely arises from trade-offs between mineral abundances and grain sizes. Figure 4 shows an example computed spectrum for a 33.3 wt % olivine-33.3 wt % enstatite-33.3 wt % anorthite mixture (pink spectrum).

In the second experiment, we use the same synthetic spectra of known mineral composition and grain sizes as in the first experiment but added an ~3% Gaussian-distributed white noise to them (e.g., medium blue spectrum in Figure 4). This experiment was designed to isolate the added errors and uncertainties associated with instrumental noise by comparison with experiment 1. While Compact Reconnaissance Orbiter Spectrometer for Mars (CRISM) noisy data are typically Poisson-distributed [e.g., *Kreisch et al.*, 2017], our intent here is not to reproduce accurate noise models for any single data set but to illustrate more generally how noise affects unmixing errors and uncertainties.

In the third experiment, we invert for composition and grain sizes of the actual, laboratory-measured mixture spectra of *Mustard and Pieters* [1987, 1989] by using optical constants derived from the endmember spectra of their experiments. Results from this experiment contain errors and uncertainties associated with nonuniqueness of the solution, inversion to optical constants with an assumed grain size, imperfections of

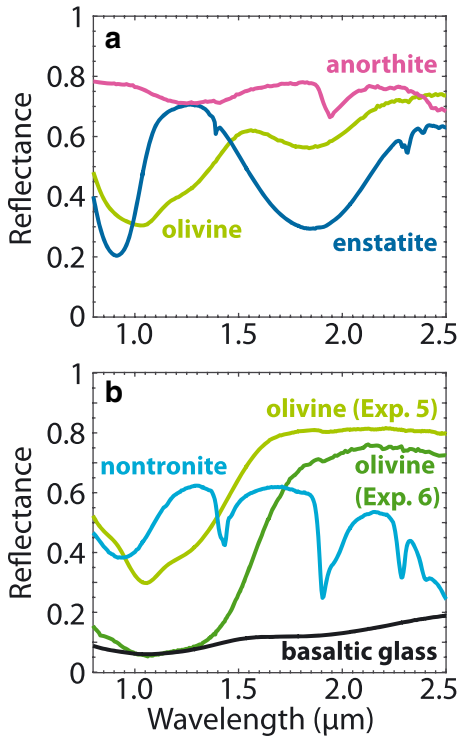

Figure 3. Reflectance spectra of mineral endmembers used for (a) the olivine/enstatite/anorthite and (b) olivine/nontronite/basaltic glass mixtures (Table 1).

the forward model, and experimental effects. Thus, comparing experiment 3 with experiment 1 (which only incorporates errors and imperfections from nonuniqueness of the solution) allows to constrain with an upper bound the systematic errors arising from the forward Hapke model (e.g., note the difference between the light blue and pink spectra in Figure 4). We note that our analysis is similar to the study of *Mustard and Pieters* [1987, 1989] with two important differences: (1) we use known grain size to derive optical constants from the endmembers rather than using endmember single-scattering albedo spectra directly in unmixing and (2) then we invert for grain sizes simultaneously with abundance, as opposed to prescribing them in the forward model. There may be some additional contributions to errors from the experiment setup, e.g., settling or sorting of grains in the sample cup; however, these were mitigated for to the greatest extent possible, as described in *Mustard and Pieters* [1987, 1989].

In a fourth experiment, we invert for composition and grain sizes of the same laboratory-measured mixtures as in the third experiment, to which we added Gaussian-distributed white noise (e.g., dark blue spectrum in Figure 4). This experiment was designed to isolate the added errors and uncertainties associated with instrumental noise by comparison with experiment 3. Thus, comparing our experiments 1–4 with those of *Mustard and Pieters* [1987] (prescribed grain sizes, $P = 1$) and *Mustard and Pieters* [1989] (prescribed grain sizes, $B = 0$, the effect of P is investigated) allows evaluation of the relative effects on inversion accuracy of noise, solution

Table 1. Reflectance Spectra Used in This Study

Suite of Mineral Endmembers	Sample Type	Spectrum ID
Olivine-enstatite-anorthite (25 spectra)	pure olivine	C1PO17[a]
	pure enstatite	C2PE12[a]
	pure anorthite	C1PA12[a]
	olivine-enstatite binary mixtures	CBXO15-19[a]
	olivine-anorthite binary mixtures	CBXO20-24[a]
	enstatite-anorthite binary mixtures	CBXA01-05[a]
	ternary mixtures	CMXO30-36[a]
Olivine-nontronite-basaltic glass (30 spectra)	pure olivine (experiment 5)	C1BE28[a]
	pure olivine (experiment 6)	HS285.4B[b]
	pure nontronite	C1BE100[a]
	pure glass	C2BE14[a]
	olivine-nontronite binary mixtures	C1BE30-136[a]
	olivine-glass binary mixtures	C1BE130-136[a]
	nontronite-glass binary mixtures	C1BE101-106[a]
	ternary mixtures	C1BE150-156[a]

[a]RELAB Brown/NASA-Keck spectral library.
[b]USGS spectral library [*Clark et al.*, 2007].

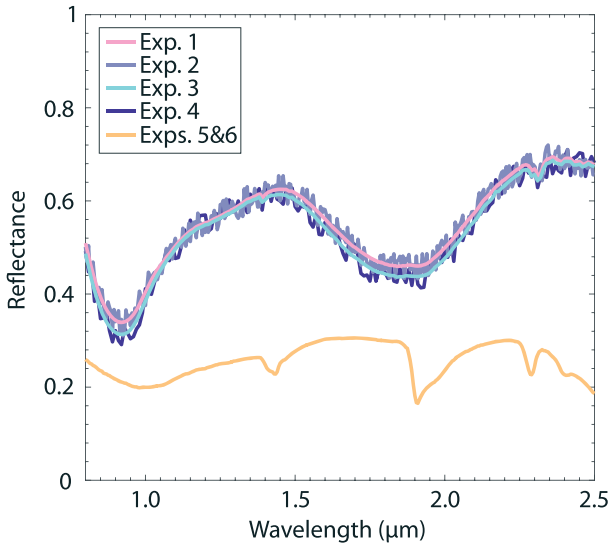

Figure 4. Example modeled MAP spectra for the 33.3%/33.3%/33.3% mixtures for all six experiments: computed mafic mixture (experiment 1; pink), computed noisy mafic mixture (experiment 2; purple), actual laboratory mafic mixture (experiment 3; light blue), actual laboratory noisy mafic mixtures (experiment 4; dark blue), and actual laboratory olivine-nontronite-glass mixture (experiments 5 and 6; orange). Note that experiments 1–4 and experiments 5 and 6 involve different endmembers, as described in the text.

nonuniqueness when both grain size and abundance are simultaneously solved for, accuracy of the physical scattering model, and prescribed photometric functions.

In the fifth experiment, we invert for composition and grain sizes of ternary laboratory mixtures of olivine, nontronite, and basaltic glass from *Ehlmann* [2010] (e.g., orange spectrum in Figure 4). This experiment is designed to illustrate the effects of added complexity (versus experiment 3), which may arise from hydrated phases with complex particle properties like nontronite [*Pilorget et al.*, 2016] and/or from phases with low spectral contrast like basaltic glass. Note that while in theory plagioclase in the mafic mixtures in experiments 1–4 is a low spectral contrast material, the particular sample used is hydrated, thus imparting spectral features of higher contrast.

Finally, in the sixth experiment, we invert for composition and grain sizes of ternary laboratory mixtures of olivine, nontronite, and basaltic glass (same as experiment 5) by using an input olivine endmember that is different from the actual olivine in the mixture (see Figure 3b). This experiment is designed to simulate a more "real-life"-like scenario, in which one does not know, a priori, the precise chemical composition of solid solutions in the target and illustrates errors and uncertainties associated with the choice of mineral endmembers and their optical constants.

Because we use three endmembers to model all mixtures, including pure and binary mixtures, the reported experiments test the ability of our algorithm to identify the absence of a mineral endmember in a geologic target. In order to also test the ability of our algorithm to identify the presence of low-spectral-contrast mineral endmembers in a geologic target (such as basaltic glass), we performed an experiment similar to experiment 5, but in which we omitted basaltic glass as an input mineral endmember. At least in the case of this particular set of minerals, modeled spectra did not fit the data, with corresponding RMS errors greater than 2% and as high as 8%, making apparent that at least one additional input mineral endmember was required. Such a procedure highlights the importance of initial iterative selection of endmembers and how an initially high RMS fit can signal missing phases (see section 2.2.1).

A seventh experiment is presented in a separate paper [*Lapotre et al.*, 2017]. In the latter, mineral composition and grain sizes of sands at the Bagnold Dunes of Gale crater, Mars, are evaluated from CRISM data and compared with ground truth measured by the Curiosity rover. This experiment, compared with the first six, incorporates the added complexity of (i) atmospheric corrections, (ii) a large number of mineral endmembers, and (iii) the unknown precise chemical composition of solid solutions.

In all six experiments herein presented, we assume that grains are spherical, isotropic scatterers, and that phase angles are moderate such that backscattering effects can be ignored. Particle shape can also influence reflectance properties [e.g., *McGuire and Hapke*, 1995; *Grundy et al.*, 2000; *Souchon et al.*, 2011; *Pilorget et al.*, 2016], but we do not investigate this effect systematically here. In all experiments, the prior distributions of grain sizes were assumed uniform over a 10–800 μm range, and prior abundances were all assumed to be 33.3 wt %, i.e., to be uniform for each mixture. Finally, the diagonal elements of the covariance $\mathbf{C}_\chi$ were taken equal to 5×10^{-4} in all experiments, a value that was visually assessed to yield a satisfying range in accepted spectra (i.e., allowing for deviations between data and model at approximately the magnitude of instrumental noise; e.g., Figure 2a). For each individual mixture (25 mixtures in each of the first four experiments and 30 mixtures in the fifth and sixth experiments), we invert for a Markov chain of 25×10^3 accepted models.

In sections 3.2–3.7, we present and discuss the results of our six experiments. To evaluate model accuracy, we use the mean error, defined as

$$\text{error} = \frac{\sum_{i=1}^{3} \left| m_{i,\text{truth}} - m_{i,\text{MAP}} \right|}{3}. \tag{23a}$$

and

$$\text{error} = \frac{\sum_{i=1}^{3} \left| D_{i,\text{truth}} - D_{i,\text{MAP}} \right|}{3}. \tag{23b}$$

as metrics for model error in abundances and grain sizes, respectively. Because all samples were sieved to 45–75 μm, we assume the true grain size, $D_{i,\text{truth}}$, to be equal to 60 μm. In the cases of pure samples or binary mixtures, where not all endmembers are present, the true grain sizes of the absent phase(s) are undefined, and equation (23b) was modified to only take into consideration those phases that are present in the sample. In addition, we use the width of the 95% confidence interval, defined as the difference between the 2.5th and 97.5th percentiles of each parameter PDFs, as a metric for uncertainty.

Two additional metrics are used to quantify errors and uncertainties integrated over all mixtures for a given set of mineral endmembers—the average mean and absolute maximum errors/uncertainties. The average mean error/uncertainty is the value of the mean error/uncertainty (mean error is as defined in equation (23)) averaged over all mixtures of a given experiment. It is thus a measure of typical errors/uncertainties one might expect from each experiment. The absolute maximum error/uncertainty is the largest discrepancy/uncertainty in either mineral abundance or grain size found across all mixtures of a given experiment for a single phase. It is thus a measure of the "worst-case" scenario, i.e., the largest errors/uncertainties one might expect from each experiment.

3.2. Experiment 1: Computed Olivine-Enstatite-Anorthite Mixtures

Figure 5 shows errors (Figures 5a and 5c) and uncertainties (Figures 5b and 5d) associated with mineral abundance and grain size predictions in the first experiment, which used computed spectra of olivine-enstatite-anorthite mixtures. Mean errors and uncertainties in calculated abundances are relatively low for all mixtures (average mean error of ~0.6 wt %, average mean uncertainty of ~7.1 wt %). The absolute maximum error in abundance remains relatively low for this entire experiment (~4.8 wt %; anorthite in a high olivine ternary mixture). Average mean error and uncertainty in grain size over all mixtures are relatively low (26 and 332 μm, respectively), but absolute maximum error (732 μm; anorthite) and uncertainty (774 μm; enstatite) are large. The largest grain size error was found in the ternary mixture with high olivine content. Grain size uncertainties are high for most mixtures. In fact, for the grain size range we permit (10–800 μm), a complete lack of sensitivity to grain size would yield an uncertainty of ~750 μm. Thus, results for the mixtures with the maximum errors and uncertainties suggest that grain size remains basically unconstrained in these cases.

Binary mixtures with low anorthite content produce the largest uncertainties in grain size. Errors in abundances are slightly higher where uncertainties in abundances are higher, which may indicate that trade-offs between abundances and grain sizes enable different, sometimes less accurate, models to produce satisfying fits to the data. We interpret this result to be caused by abundance-grain size trade-offs for the two mafic mineral endmembers.

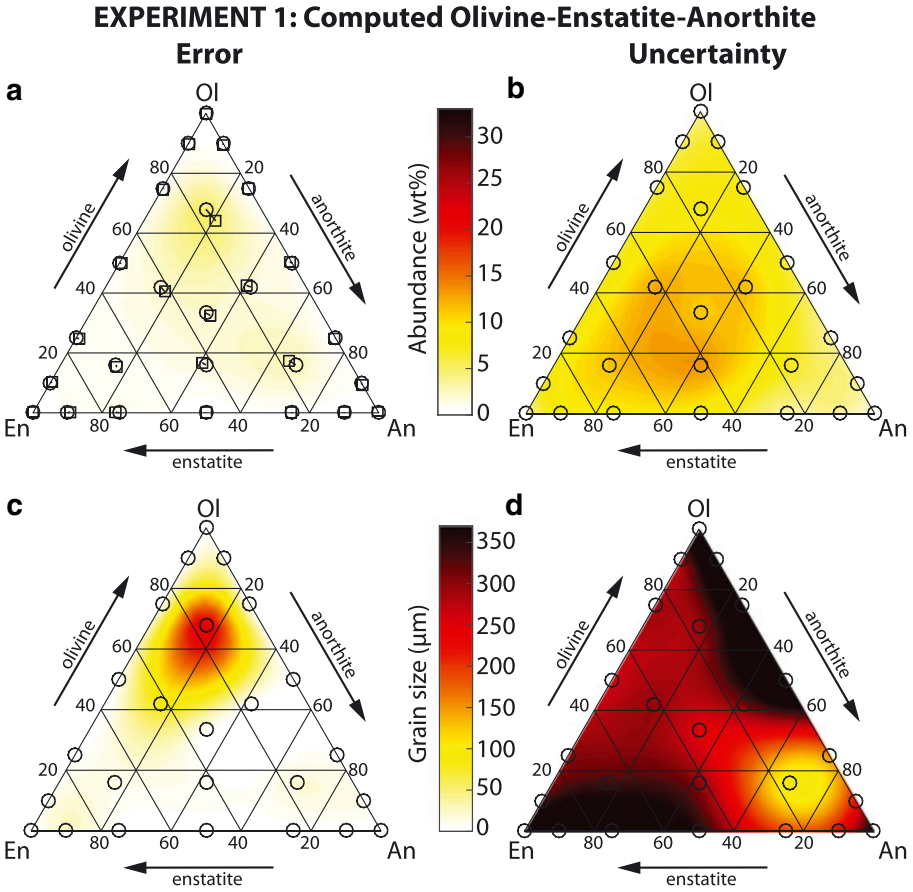

Figure 5. Experiment 1. Ternary plot of (a and c) mean error in abundance and grain size and (b and d) mean uncertainty in abundance and grain size. In Figure 5a, the open circles indicate the true compositions corresponding to the input spectra, while the open squares indicate their corresponding modeled composition. The solid lines are drawn between true and modeled compositions to avoid confusions when errors are large.

As a sensitivity analysis, we performed the same experiment for synthetic mixtures corresponding to 500 μm grains (compared with 60 μm in experiment 1). Resulting errors and uncertainties were overall statistically indistinguishable from those of experiment 1.

3.3. Experiment 2: Noisy, Computed Olivine-Enstatite-Anorthite Mixtures

Figure 6 shows errors (Figures 6a and 6c) and uncertainties (Figures 6b and 6d) associated with mineral abundances and grain sizes in the second experiment, which used the computed spectra of experiment 1 with additional, simulated random noise. Average mean error in calculated abundances is slightly higher than in experiment 1 (~1.3 wt %), but average mean uncertainty is about the same (~7.1 wt %). The absolute maximum error and uncertainty in abundance are ~6.7 wt % (anorthite in a 42 wt % olivine-16 wt % enstatite-42 wt % anorthite mixture) and ~15.8 wt % (anorthite in a 75 wt % enstatite-25 wt % anorthite mixture), respectively. Errors and uncertainties in abundances are roughly homogeneously distributed across the ternary diagram with subtly higher values for ternary mixtures than binary mixtures. Average mean error in grain size is also higher than for experiment 1 (56 μm), but average mean uncertainty is similar (~338 μm). Patterns in errors and uncertainties for grain size are overall similar to those of experiment 1. Absolute maximum error (733 μm) and uncertainty (775 μm) in grain size both occur for anorthite and reflect a lack of sensitivity to anorthite grain size for binary mixtures with low anorthite content.

Compared with experiment 1, noise in the data appears to have approximately doubled errors but left uncertainties unchanged. The abundance/grain size trade-off observed in Figure 5 for high-olivine ternary mixtures is not readily apparent in Figure 6, most likely due to noise increasing the number of acceptable models, effectively smearing the correlation between abundance and grain size.

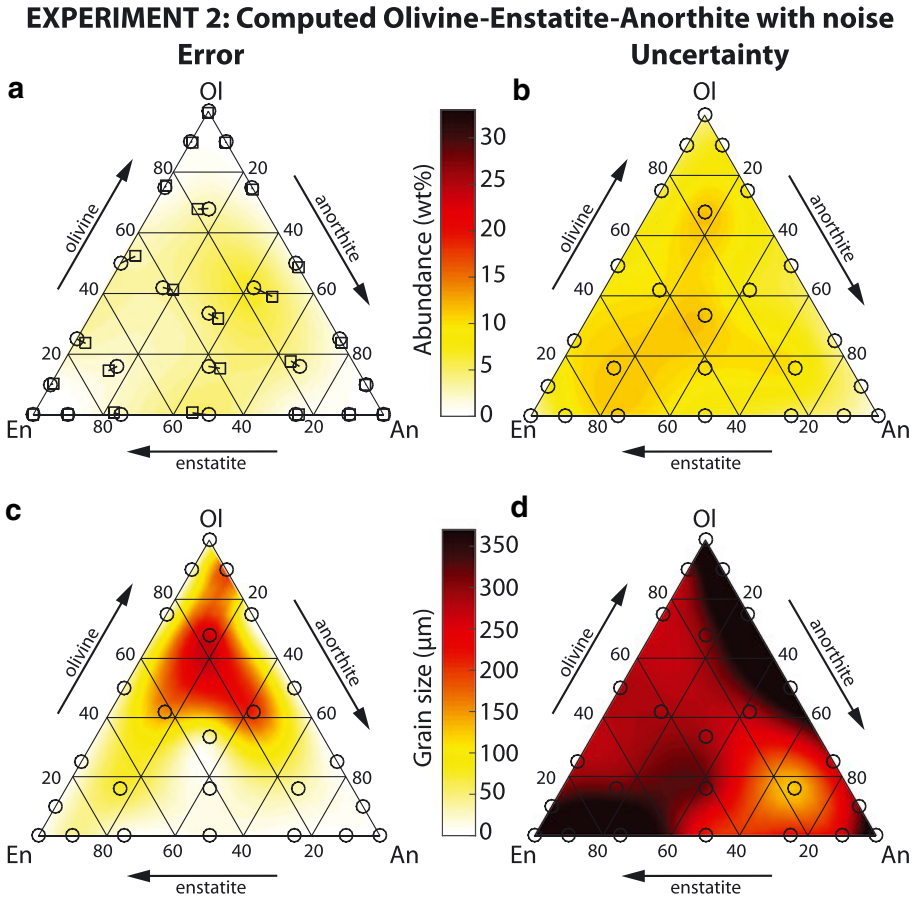

Figure 6. Experiment 2. Ternary plot of (a and c) mean error in abundance and grain size and (b and d) mean uncertainty in abundance and grain size. In Figure 6a, the open circles indicate the true compositions of the input spectra herein inverted, while the open squares indicate their corresponding modeled composition. The solid lines are drawn between true and modeled compositions to avoid confusions when errors are large.

3.4. Experiment 3: Laboratory-Measured Olivine-Enstatite-Anorthite Mixtures

Figure 7 shows errors (Figures 7a and 7c) and uncertainties (Figures 7b and 7d) associated with mineral abundances and grain sizes in the third experiment, for which we performed unmixing of actual, laboratory-measured mixture spectra. Average mean errors and uncertainties in abundances increase relative to experiments 1 and 2 (to ~2.5 wt % and ~8.9 wt %, respectively). The absolute maximum error corresponds to a 90% olivine and 10% anorthite binary mixture, with an ~13.3 wt % error in olivine (and a >12 wt % error in anorthite). The absolute maximum uncertainty in abundance occurs for a binary mixture (~20.9 wt % for anorthite in a 75 wt % enstatite-25 wt % anorthite mixture). Average mean error and uncertainty in grain size are of 69 and 374 μm, respectively. Similar to experiments 1 and 2, mixtures with low anorthite contents yielded less accurate grain sizes, with an absolute maximum error of 680 μm occurring for anorthite in a 90 wt % olivine-10 wt % anorthite mixture showing a complete lack of sensitivity to anorthite grain size for those mixtures (absolute maximum uncertainty of 747 μm). Interestingly, grain size uncertainties are lowest for mixtures with olivine and enstatite mixed in roughly equal proportions.

Figure 8 shows how error and uncertainty for individual minerals vary with the actual abundance of that same mineral in the mixture for experiment 3. For these specific endmembers and mixtures, enstatite is generally more accurately (lower error) predicted for low enstatite content, anorthite for high anorthite content, and olivine for intermediate olivine contents (Figures 8a and 8b). For all three phases, abundance is more certainly (lower uncertainty) determined when the mineral is either absent or alone in the sample; i.e., the modeled composition is more likely to be accurate for mixtures dominated by a single phase (Figures 8e and 8f). Grain size errors and uncertainties exhibit a completely different dependence on abundance and are

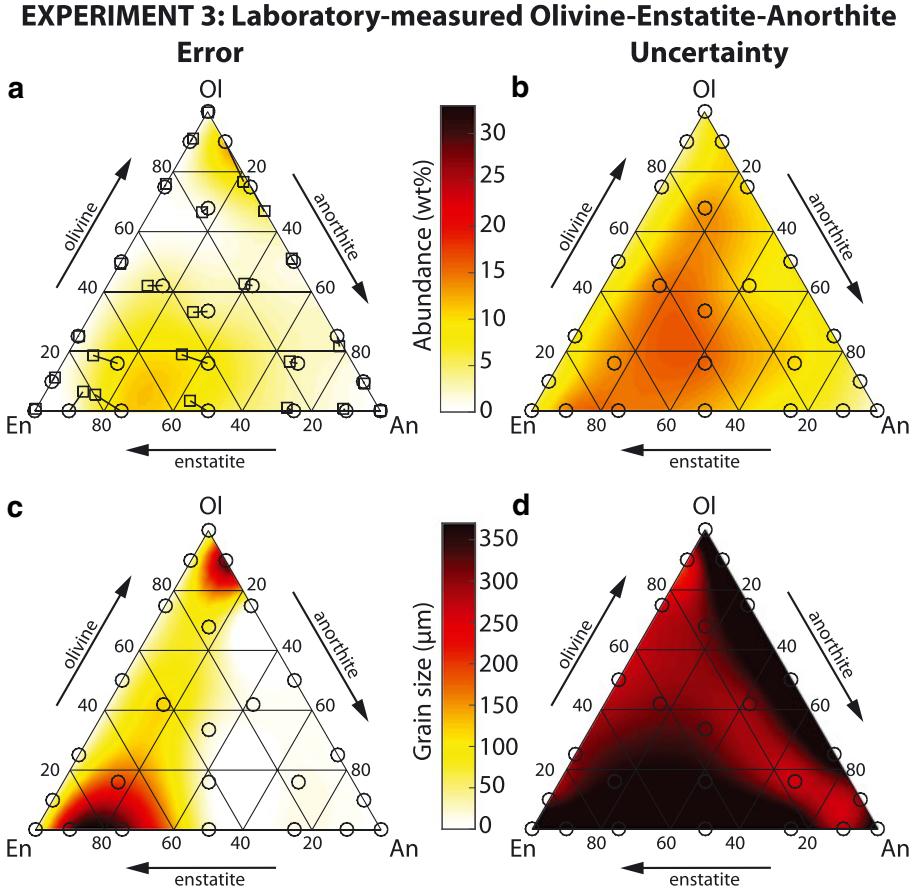

Figure 7. Experiment 3. Ternary plot of (a and c) mean error in abundance and grain size and (b and d) mean uncertainty in abundance and grain size. In Figure 7a, the open circles indicate the true compositions of the input spectra herein inverted, while the open squares indicate their corresponding modeled composition. The solid lines are drawn between true and modeled compositions to avoid confusions when errors are large.

highest when the abundance of the phase is low (Figures 8c and 8d and 8g and 8h). Grain sizes of anorthite are notably the most inaccurately and uncertainly determined, even at intermediate-to-high anorthite contents. Indeed, despite being hydrated, the anorthite sample has a relatively low spectral contrast, such that erroneous grain sizes do not significantly affect the spectral fit.

We find that errors in modeled abundances roughly double when grain sizes are left as free parameters and optical constants are used (experiment 3 versus *Mustard and Pieters* [1987, 1989], in which grain size was a fixed parameter and unmixing was based solely on endmember single-scattering albedo spectra) and that systematic errors in abundances arising from either systematic errors in the forward model or experiment effects (e.g., settling of mineral grains in sample cup) are about 4 times those associated with solution nonuniqueness alone (experiment 3 versus experiment 1).

3.5. Experiment 4: Noisy Laboratory-Measured Olivine-Enstatite-Anorthite Mixtures

Figure 9 shows errors (Figures 9a and 9c) and uncertainties (Figures 9b and 9d) associated with mineral abundances and grain sizes in the fourth experiment, which used laboratory-measured spectra with simulated, random noise. Average mean error in calculated abundances is slightly higher than in experiment 3 (~2.8 wt %), but average mean uncertainty is similar (~8.8 wt %). The absolute maximum error and uncertainty in abundance are both found to correspond to anorthite and are ~15.1 wt % (in a 16 wt % olivine-68 wt % enstatite-16 wt % anorthite mixture) and ~21.0 wt % (in a 42 wt % olivine-16 wt % enstatite-42 wt % anorthite mixture), respectively. Patterns in errors and uncertainties in abundances are very similar to those of experiment 3. Average mean error in grain size is also higher than for experiment 3 (97 μm), but average

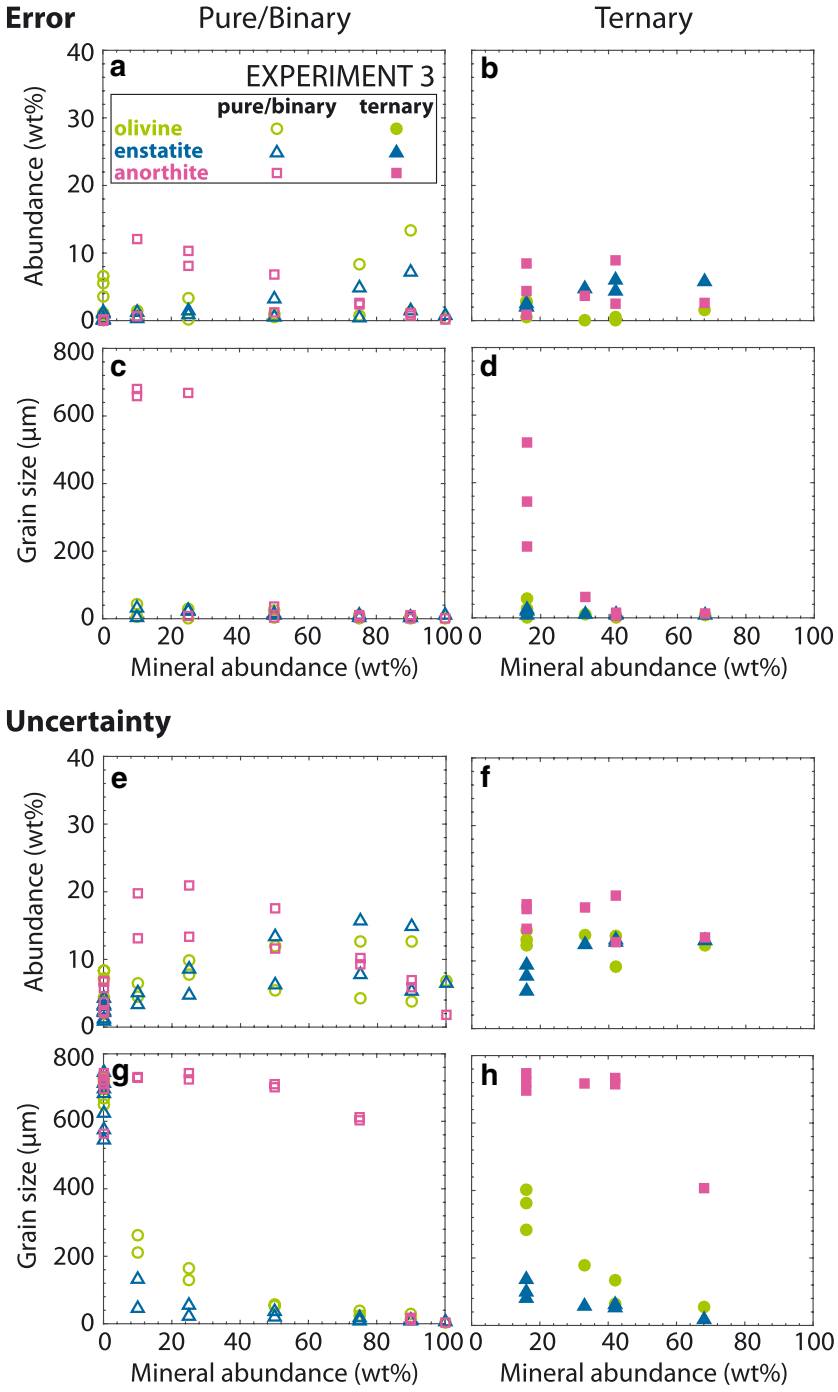

Figure 8. Experiment 3. Variations in (a–d) error and (e–h) uncertainty as a function of the actual corresponding mineral abundances for olivine (green circles), enstatite (blue triangles), and anorthite (pink squares) abundances (Figures 8a and 8b and 8e and 8f) and grain sizes (Figures 8c and 8d and 8g and 8h), respectively. Pure samples and binary mixtures (Figures 8a, 8c, 8e, and 8g) are denoted by open symbols, while ternary mixtures (Figures 8b, 8d, 8f, and 8h) are denoted by filled symbols.

mean uncertainty is similar (~368 μm). Absolute maximum error (722 μm, in a 16 wt % olivine-68 wt % enstatite-16 wt % anorthite mixture) and uncertainty (771 μm, in a 90 wt % olivine-10 wt % anorthite mixture) in grain size both occur for anorthite and reflect a complete lack of sensitivity to grain size for binary mixtures with anorthite.

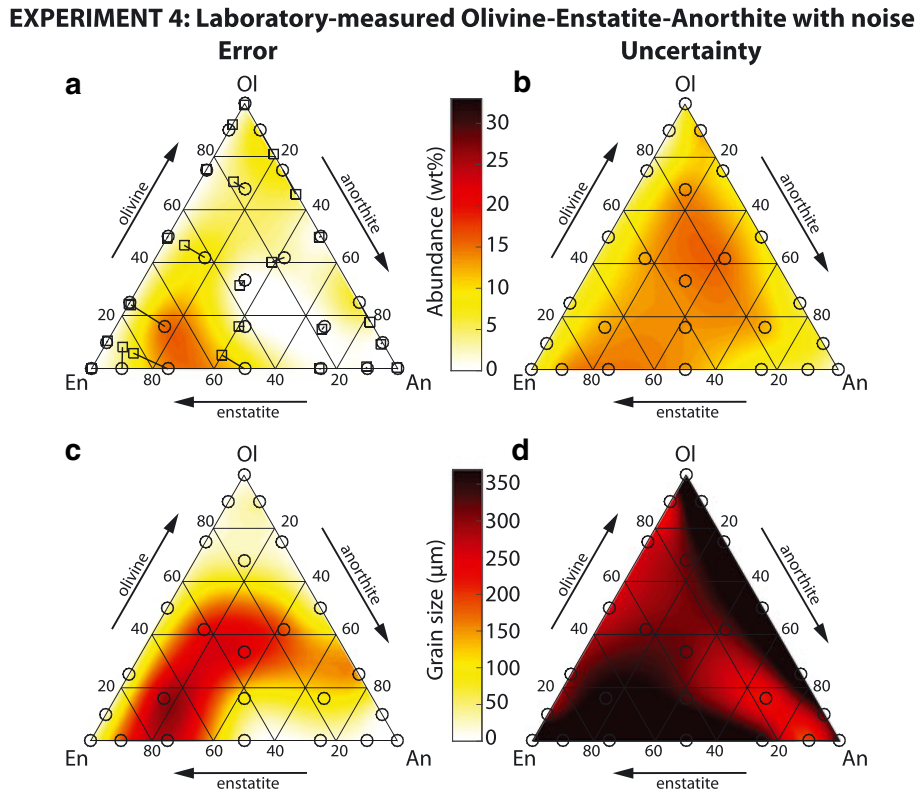

Figure 9. Experiment 4. Ternary plot of (a and c) mean error in abundance and grain size and (b and d) mean uncertainty in abundance and grain size. In Figure 9a, the open circles indicate the true compositions of the input spectra herein inverted, while the open squares indicate their corresponding modeled composition. The solid lines are drawn between true and modeled compositions to avoid confusions when errors are large.

Compared with experiment 3, noise in the data slightly increased errors but left uncertainties unchanged. Finally, the similarities between experiments 1–4 (e.g., Figures 5–9) provide confidence that the observed trends are intrinsic to the minerals investigated here and to the Hapke forward model, as opposed to nonreproducible patterns associated with randomness from our Bayesian approach.

3.6. Experiment 5: Laboratory Olivine-Nontronite-Glass Mixture

Figure 10 shows errors (Figures 10a and 10c) and uncertainties (Figures 10b and 10d) associated with mineral abundances and grain sizes in the fifth experiment, where we performed unmixing of actual, laboratory-measured spectra from a different ternary mixture suite with a low contrast phase (glass). Average mean errors and uncertainties in abundances are yet higher for this set of mineral endmembers than for those of experiment 4 (~5.6 wt % and ~17.2 wt %, respectively). Absolute maximum error occurs for nontronite (~22.8 wt %, in a 42 wt % olivine-42 wt % nontronite - 16 wt % glass mixture), and absolute maximum uncertainty occurs for olivine (~48.9 wt % in a 30 wt % olivine-70 wt % glass mixture). Errors and uncertainties in abundances are generally lower along the olivine-nontronite join and roughly increase as glass content increases. Errors in grain sizes appear to be higher for nontronite-glass binary mixtures of high nontronite content. Average mean error and uncertainty in grain sizes are of 59 μm and 313 μm, respectively. Absolute maximum error in grain size occurs for basaltic glass (700 μm, in a 90 wt % olivine-10 wt % glass mixture), and absolute maximum uncertainty occurs for olivine (775 μm, for a 100 wt % nontronite sample).

Figure 11 shows how error and uncertainty for a given mineral vary with the actual abundance of that same mineral in the mixture. Errors and uncertainties in abundance are sometimes large when a mineral is absent or dominant in the mixture (e.g., no olivine and 95% basaltic glass; Figures 11a and 11e) but are typically highest at intermediate contents (Figures 11a and 11b and 11e and 11f). Olivine errors generally decrease at high olivine contents. Interestingly, while uncertainties in olivine and nontronite abundances generally decrease with increasing abundance, the opposite trend is observed for basaltic glass (Figures 11e and 11f). Trends

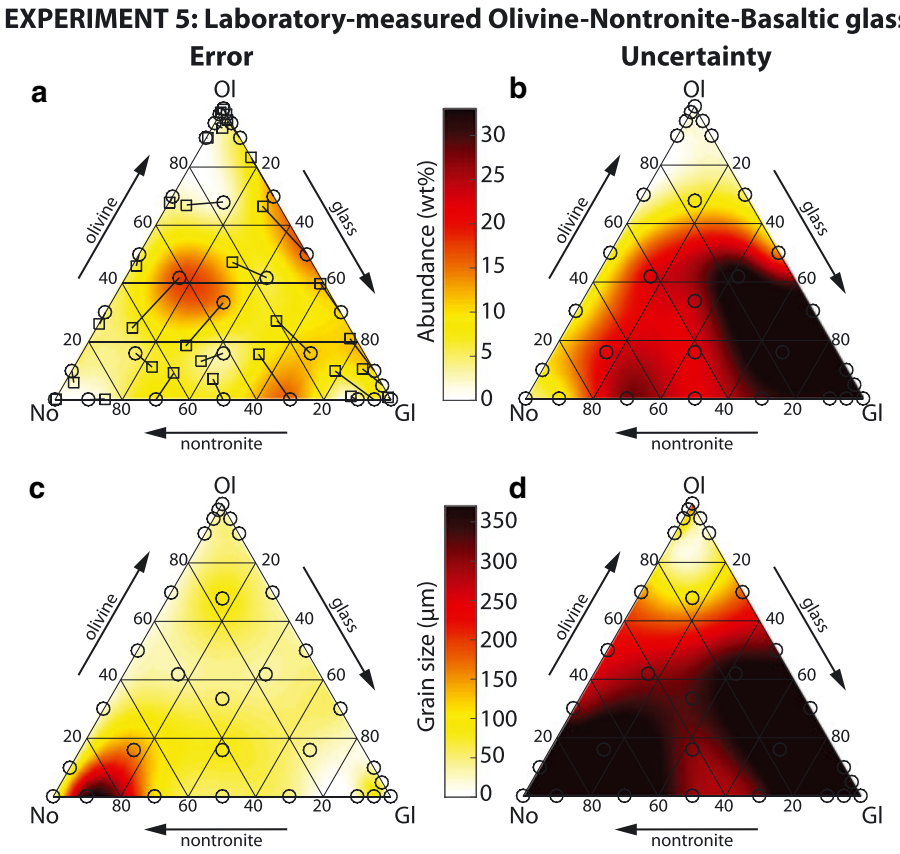

Figure 10. Experiment 5. Ternary plot of (a and c) mean error in abundance and grain size and (b and d) mean uncertainty in abundance and grain size. In Figure 10a, the open circles indicate the true compositions of the input spectra herein inverted, while the open squares indicate their corresponding modeled composition. The solid lines are drawn between true and modeled compositions to avoid confusions when errors are large.

in errors and uncertainties in grain sizes remain similar to those of experiment 3, with error for a given constituent decreasing with increasing abundance of the phase (Figures 11c and 11d and 11g and 11h). The effect is most remarkable for basaltic glass, which has a very large error in grain size at low abundance.

The highest errors in abundance and uncertainties in both abundance and grain size occur for low olivine and nontronite but high glass contents. Basaltic glass, which has a low spectral contrast in this wavelength range (e.g., Figure 3), is thus the likely dominant cause of errors and uncertainties in mineral abundances for this mixture suite, rather than abundance/grain size trade-offs for a given endmember, which was more important in experiment 3. Thus, comparing experiments 3 and 5 highlights the specific challenges of certain mineral assemblages.

3.7. Experiment 6: Laboratory Olivine-Nontronite-Glass Mixture With a Different Olivine Endmember Optical Constant

In the sixth experiment, we test the effect of discrepancies between the optical constants of mineral endmembers in the target and those used in the inversion. In particular, we investigate the scenario of using an olivine with a different imaginary index of refraction in our forward model (Figure 12 and Table 1). Figure 13 shows errors (Figures 13a and 13c) and uncertainties (Figures 13b and 13d) associated with mineral abundances and grain sizes in the sixth experiment. While the average mean error in abundances is higher than in experiment 5 (~8.6 wt %), the average mean uncertainty is lower (~15.8 wt %). Absolute maximum error and uncertainty both occur for nontronite (~31.9 wt % and ~41.4 wt %, respectively). Patterns in abundance uncertainties are very similar to those observed in experiment 5. Similarly, patterns in grain size errors and uncertainties are very similar to those of experiment 5. Average mean error and uncertainty in grain sizes are of 64 μm and 335 μm, respectively. Absolute maximum error in grain size occurs for basaltic glass

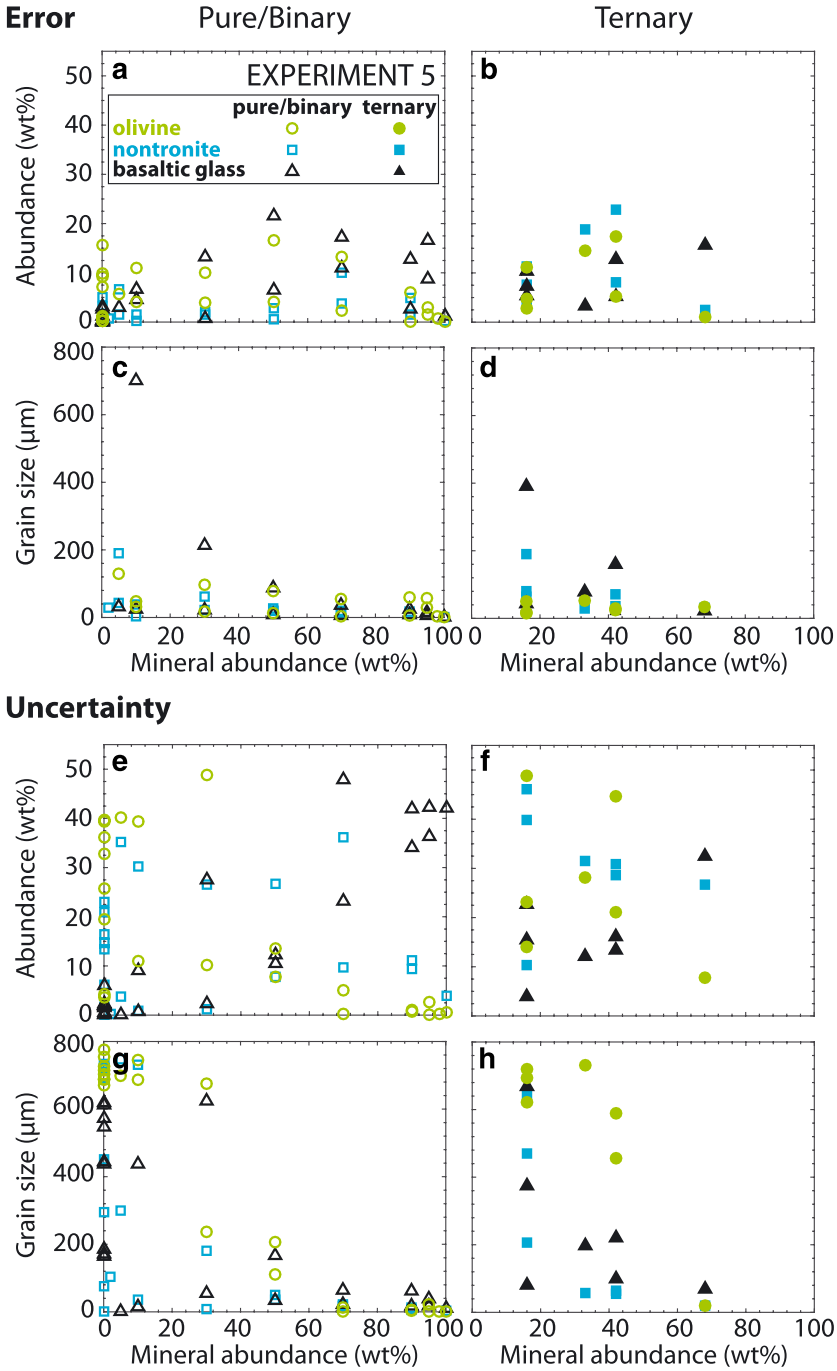

Figure 11. Experiment 5. Variations in (a–d) error and (e–h) uncertainty as a function of the actual corresponding mineral abundance for olivine (green circles), nontronite (blue squares), and glass (black triangles) abundances (Figures 11a and 11b and 11e and 11f) and grain sizes (Figures 11c and 11d and 11g and 11h), respectively. Pure samples and binary mixtures (Figures 11a, 11c, 11e, and 11g) are denoted by open symbols, while ternary mixtures (Figures 11b, 11d, 11f, and 11h) are denoted by filled symbols.

(702 μm, in a 90 wt % nontronite-10 wt % glass mixture), and absolute maximum uncertainty occurs for olivine (766 μm, in a 16 wt % olivine-16 wt % nontronite-68 wt % glass mixture).

The main difference between experiments 5 and 6 is that errors in abundance increase, but corresponding uncertainties decrease. We interpret this trend as the result of a generally poorer fit to the data due to the

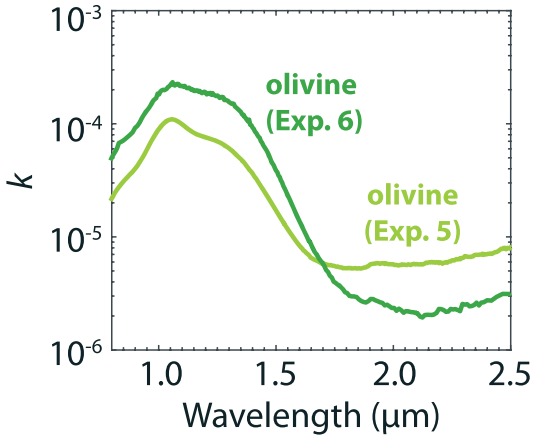

Figure 12. Imaginary index of refraction of the olivine endmember we use in experiment 6 compared with that of the true olivine in the mixture (and used in experiment 5).

different olivine (higher error) but fewer mineral assemblages yielding acceptable fits (lower uncertainty). Errors in abundance are now clearly highest for mixtures with moderate amounts of olivine.

4. Discussion

Figure 14 summarizes the average mean and absolute maximum errors and uncertainties in abundance and grain size for all six experiments. Overall, average errors between MAP modeled compositions and true compositions are low for both mixtures investigated (<10 wt % abundance; <100 μm in grain size). However, specific mixtures can be more prone to trade-offs between mineral abundances and grain sizes or have low spectral contrast endmembers, such that relatively large errors may arise (e.g., up to ~32 wt % for one endmember for one mixture in experiment 6).

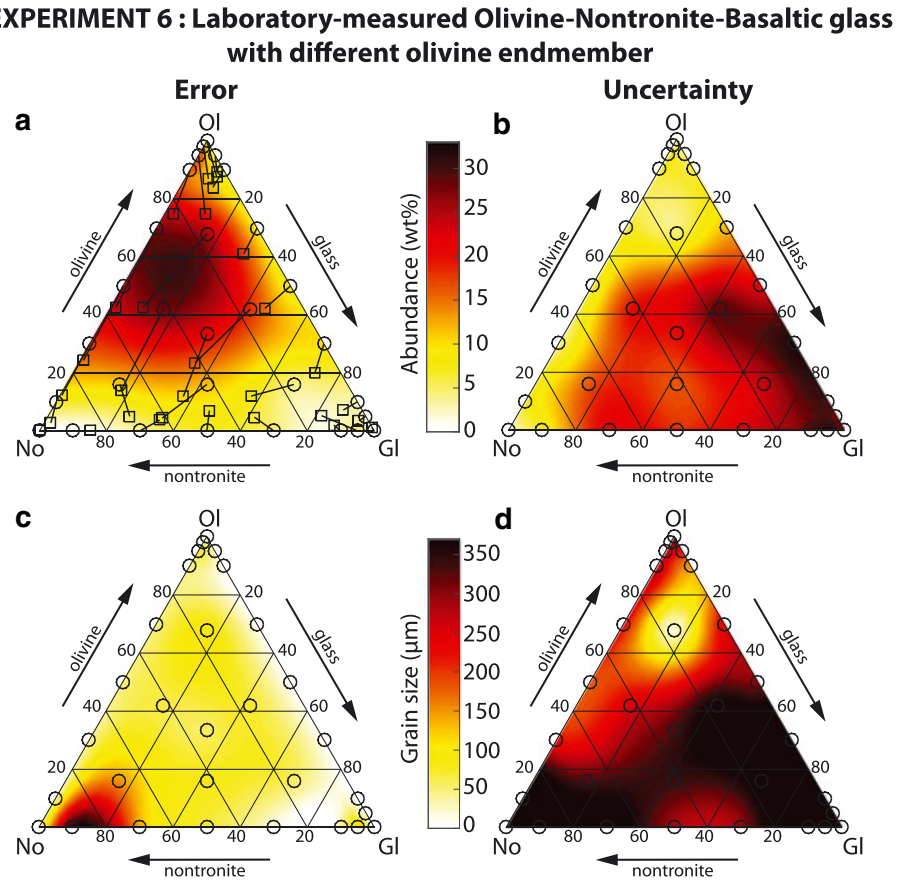

Figure 13. Experiment 6. Ternary plot of (a and c) mean error in abundance and grain size and (b and d) mean uncertainty in abundance and grain size. In Figure 13a, the open circles indicate the true compositions of the input spectra herein inverted, while the open squares indicate their corresponding modeled composition. The solid lines are drawn between true and modeled compositions to avoid confusions when errors are large.

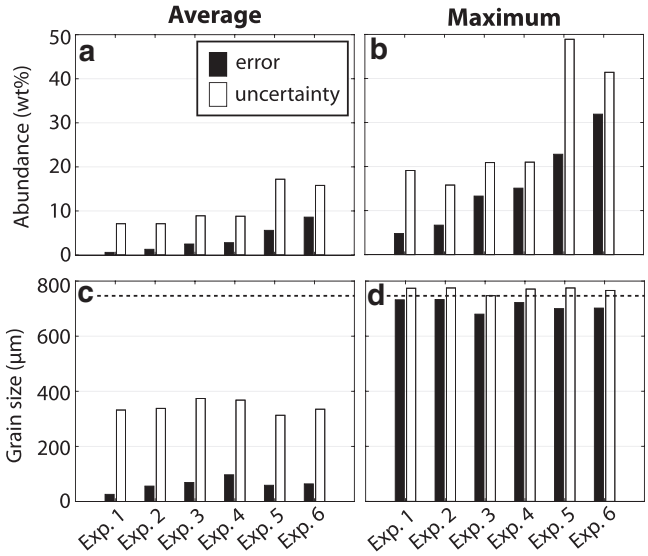

Figure 14. Summary of experiments 1–6. (a and c) Average mean and (b and d) absolute maximum errors (black) and uncertainties (white) of inverted mineral abundances and grain sizes, respectively. The dashed line in Figures 14c and 14d represents the expected uncertainty for uniform grain size distributions over the allowed range, i.e., the uncertainty corresponding to a complete lack of sensitivity of the model on grain size.

Overall, through these six experiments, we showed the following:

1. Spectral unmixing with the Hapke model provides weak constraints on grain size (experiment 1 and all others). In general, uncertainty on derived grain sizes is large, and there is little sensitivity to grain size for most phases with low abundances.
2. The inherent nonuniqueness of the solution alone, due to trade-offs between abundance and grain size, leads to typical errors $<$ ~5 wt % in abundance for mafic mixtures (experiment 1).
3. An ~3% noise in the data increases errors by up to ~2 wt % (experiments 1 versus 2 and experiments 3 versus 4).
4. The particular trade-offs leading to errors and uncertainties are intrinsic to the mineral phases in the mixture (experiments 3 versus 5). For example, the presence of low spectral contrast phases such as basaltic glass may further decrease the accuracy of the inversion technique.
5. Unmixing of laboratory data as opposed to synthesized data increases errors in abundance by a factor of ~4. Thus, if this is due to systematic errors associated with the forward physical model and assumptions therein, were a perfect model to exist, errors in abundance could be reduced by a factor of ~4 (experiments 1 versus 3). However, uncertainties remain high due to nonuniqueness of the inverse problem. Additional experiments and characterization of samples surfaces might reveal if this were instead an experimental artifact (e.g., settling of certain composition grains away from the optical surface).
6. Using slightly inaccurate optical constants may lead to an increase in abundance error (of ~3 wt % in the case of experiment 6 versus experiment 5) but a decrease in abundance uncertainty (of ~1.5 wt %), due to fewer assemblages yielding acceptable fits to the data.

Our results have significant implications for the use of spectral unmixing of VSWIR remote sensing data. First, the Hapke model best fit can be highly accurate ($<$1 wt % error) and, indeed, is accurate ($<$10 wt % error) on average. This is true even in the face of significant noise, which slightly increases error but does not appreciably change uncertainty. However, the high magnitude of errors in abundance unmixing results (20–30 wt %) observed for a small subset of mixtures might lead to incorrect conclusions about composition and thus active geologic processes. Most worrisome is the fact that which mixtures/planetary surfaces will exhibit high errors cannot fully be predicted. One cause for higher errors appears to be low spectral contrast phases, the presence of which is hard to know a priori. A second cause for higher errors may be more tractable: inherent nonuniqueness in fits as the effects of mineral abundance and grain sizes trade-off within the permitted range of model misfit. Our model results show greater abundance errors than *Mustard and Pieters* [1987] for their mixtures because they constrain grain size while we do not. This emphasizes a key role that

independent constraints on grain size—e.g., from thermal inertia [e.g., *Liu et al.*, 2016] or from geologic context [e.g., *Lapotre et al.*, 2017]—can have in effectively minimizing the errors in unmixing data. Altogether, our results highlight the importance of calculating uncertainties on unmixing model fits and considering the geological implications of the full range of permitted solutions, rather than interpretations relying on a sole acceptable solution. Our overall recommendation is to report both the MAP and the full 95% confidence interval (or whatever confidence interval is desired) to properly acknowledge the relatively high uncertainties from spectral unmixing [e.g., *Lapotre et al.*, 2017].

Additional work might examine the above points (4)–(6) through additional laboratory experiments with constituent mixtures relevant to planetary surfaces. In particular for (5), efforts should be made to independently characterize optical surfaces when acquiring spectral data (e.g., by photography or microimaging spectroscopy) to definitively separate systematic errors in the construction of the forward model from experimental effects, thus enabling the formulation of improved radiative transfer models.

5. Conclusions

Reflected light in the VSWIR wavelength range provides key information on surface composition, and mineral/mineraloid/ice/organic abundances and grain sizes can be estimated from spectral unmixing. Nevertheless, our data sets demonstrated that solutions to the quantitative inverse problem are nonunique and highlight the need for more sophisticated unmixing approaches that simultaneously obtain both a best fit and the range of uncertainty, which includes consideration of multiple permitted solutions. Our combined Hapke model with MCMC sampler illustrated the effects of inherent trade-offs between abundance and grain size, noise in the data, likely systematic model errors, the precise suite of mineral endmembers present, and choice of optical constants. We find that spectral unmixing is only weakly and selectively sensitive to grain size, with virtually no sensitivity to grain size at all for phases with low abundances in the mixtures investigated here. For synthesized spectra of the particular mixture compositions examined, trade-offs between mineral abundances and grain sizes lead to typical errors in the inverted abundances of ~1 wt % (maximum 5 wt %), while instrumental noise may increase them by up to ~2 wt %. When actual laboratory data are examined, errors increase by a factor of ~4, likely associated with systematic errors in the forward model, though experimental artifacts cannot be excluded as a contributor to the error. In general, inverted mineral abundances are most accurate and certain when a given mineral is either present at minor abundances or alone in a mixture, while accuracy and certainty in inverted grain sizes increase with the relative abundance of corresponding minerals. For our olivine-nontronite-basaltic glass mixture, we found that typical errors are even higher, generally ~6 wt % but up to ~23 wt % due to the presence of the relatively featureless, low spectral contrast basaltic glass. We also find that using slightly inaccurate optical constants may increase errors but decrease uncertainties in abundances, due to fewer mineral assemblages fitting the data. Overall, we find that uncertainties associated with spectral unmixing are large. These large uncertainties emphasize the need for (i) more laboratory-based studies encompassing more mineral phases and larger grain-size ranges and (ii) a probabilistic approach to spectral unmixing that allows characterizing the likelihood of sets of mineral assemblages, and as such, characterizes the degree of confidence with which one may interpret spectral data in terms of surface composition.

Notations

$\mathbf{a}$	Concentration parameters for the Dirichlet distribution
B	Backscattering function
B	Multinomial beta function
$\mathbf{C}_\chi$	Covariance matrix
$\mathbf{d}$	Spectral data
$\mathbf{D}$	Grain sizes (μm)
$\langle D \rangle$	Mean free path (m)
Dir	Dirichlet distribution
$\mathbf{e}$	Measurement error
f	Mineral relative cross section
g	Phase angle

G	Deterministic forward model
H	Chandrasekhar integral function
J	Number of transitional PDFs in CATMIP [e.g., *Minson et al.*, 2013]
k	Imaginary refractive index
L	Length of the Markov chain
$\mathbf{m}$	Mineral abundances (wt %)
n	Real refractive index
N	Number of mineral endmembers
N_d	Number of wavelengths/ single-scattering albedo pairs in the data
p	Probability
P	Phase function
r	Reflectance
r_0	Bihemispherical reflectance for isotropic scatterers
r_i	Internal bihemispherical reflectance in a particle
s	Volume scattering coefficient inside a particle
S_e	Surface reflection coefficient for externally incident light
S_i	Reflection coefficient for internally scattered light
u	Random draw from the standard uniform distribution, $U(0, 1)$
U	Uniform distribution
w	Single-scattering albedo
x	Generic variable
y	Candidate sample for the Markov chain
z	Random draw from a zero-mean multivariate normal distribution
α	Internal absorption coefficient
β	Tempering parameter for CATMIP [e.g., *Minson et al.*, 2013]
γ	$\sqrt{(1-w)}$
Γ	Gamma function
$\boldsymbol{\delta}$	Measurement predictions
$\boldsymbol{\varepsilon}$	Model prediction errors
η	Mean of $(\mathbf{e}+\boldsymbol{\varepsilon})$
$\boldsymbol{\theta}$	Set of model parameters
Θ	Particle internal transmission coefficient
λ	Wavelength of light (μm)
μ	Cosine of the light emergence angle
μ_0	Cosine of the light incidence angle
ρ	Mineral density (kg/m^3)
σ	Mineral cross section (m^2)
Σ	Covariance of proposal PDF in CATMIP [e.g., *Minson et al.*, 2013]
ϕ	$\min\left\{1, \frac{p(\mathbf{y}\|\mathbf{d})}{p(\boldsymbol{\theta}_i\|\mathbf{d})}\right\}$

Acknowledgments

We thank Ryan Anderson and Tim Titus of the U.S. Geological Survey for their comments, and Yang Liu and William Farrand for their constructive reviews of our manuscript. We also thank James Beck for early discussions on MCMC methods. This research utilizes spectra acquired by Carle Pieters, John Mustard, and Bethany Ehlmann with the NASA/Keck RELAB facility at Brown University. All MATLAB scripts to run the MCMC procedure are available for download at http://resolver.caltech.edu/CaltechAUTHORS:20170302-115016869. M.G.A.L. was partially funded by a NASA Earth and Space Science Fellowship (12-PLANET12F-0071) and from a MSL Participating Scientist Program grant to B.L.E. We acknowledge the support of a NASA PGG grant to John Mustard for acquisition of mixture data for experiments 5 and 6. Laboratory spectra presented in this paper are available in the RELAB Brown/NASA-Keck spectral library.

References

Bayes, M. (1763), An essay towards solving a problem in the doctrine of chances, *Philos. Trans. R. Soc.*, *53*, 370–418.

Beck, J. L., and S. K. Au (2002), Bayesian updating of structural models and reliability using Markov chain Monte Carlo simulation, *J. Eng. Mech.*, *128*(4), 380–391, doi:10.1061/(ASCE)0733-9399.

Beck, J. L., and K. M. Zuev (2013), Asymptotically independent Markov sampling: A new MCMC scheme for Bayesian inference, *Int. J. Uncertainty Quantification*, *3*(5), 445–474.

Burns, R. G. (1993), Rates and mechanisms of chemical weathering of ferromagnesian silicate minerals on Mars, *Geochim. Cosmochim. Acta*, *57*(19), 4555–4574.

Cheek, L. C., and C. M. Pieters (2014), Reflectance spectroscopy of plagioclase-dominated mineral mixtures: Implications for characterizing lunar anorthosites remotely, *Am. Mineral.*, *99*(10), 1871–1892, doi:10.2138/am-2014-4785.

Chib, S., and E. Greenberg (1995), Understanding the metropolis-hastings algorithm, *The American Statistician*, *49*(4), 327–335.

Ching, J., and Y.-C. Chen (2007), Transitional Markov chain Monte Carlo method for Bayesian model updating, model class selection, and model averaging, *J. Eng. Mech.*, *133*(7), 816–832, doi:10.1061/(ASCE)0733-9399.

Clark, R. N. (1999), Spectroscopy of rocks and minerals, and principles of spectroscopy, in *Manual of Remote Sensing*, vol. 3, edited by A. N. Renz, pp. 3–58, John Wiley, New York.

Clark, R. N., and T. L. Roush (1984), Reflectance spectroscopy: Quantitative analysis techniques for remote sensing applications, *J. Geophys. Res.*, *89*(B7), 6329–6340, doi:10.1029/JB089iB07p06329.
Clark, R. N., G. A. Swayze, R. Wise, K. E. Livo, T. M. Hoefen, R. F. Kokaly, and S. J. Sutley (2007), *USGS Digital Spectral Library splib06a*, edited, U.S. Geol. Surv., Reston, Va. [Available at https://speclab.cr.usgs.gov/spectral.lib06/.]
Cruikshank, D. P., T. L. Roush, and F. O. Poulet (2003), Quantitative modeling of the spectral reflectance of Kuiper belt objects and centaurs, *C. R. Phys.*, *4*(7), 783–789, doi:10.1016/j.crhy.2003.10.007.
De Sanctis, M. C., et al. (2016), Bright carbonate deposits as evidence of aqueous alteration on (1) Ceres, *Nature*, *536*(7614), 54–57, doi:10.1038/nature18290.
Edwards, C. S., and B. L. Ehlmann (2015), Carbon sequestration on Mars, *Geology*, *43*(10), 863–866, doi:10.1130/G36983.1.
Ehlmann, B. L. (2010), Early Mars environments revealed through near-infrared spectroscopy of alteration minerals, PhD dissertation, Brown Univ.
Feely, K. C., and P. R. Christensen (1999), Quantitative compositional analysis using thermal emission spectroscopy: Application to igneous and metamorphic rocks, *J. Geophys. Res.*, *104*(E10), 24,195–24,210, doi:10.1029/1999JE001034.
Goudge, T. A., J. F. Mustard, J. W. Head, M. R. Salvatore, and S. M. Wiseman (2015), Integrating CRISM and TES hyperspectral data to characterize a halloysite-bearing deposit in Kashira crater, Mars, *Icarus*, *250*, 165–187, doi:10.1016/j.icarus.2014.11.034.
Grundy, W. M., S. Douté, and B. Schmitt (2000), A Monte Carlo ray-tracing model for scattering and polarization by large particles with complex shapes, *J. Geophys. Res.*, *105*(E12), 29,291–29,314, doi:10.1029/2000JE001276.
Hapke, B. (1981), Bidirectional reflectance spectroscopy: 1. Theory, *J. Geophys. Res.*, *86*(B4), 3039–3054, doi:10.1029/JB086iB04p03039.
Hapke, B. (1984), Bidirectional reflectance spectroscopy: 3. Correction for macroscopic roughness, *Icarus*, *59*(1), 41–59.
Hapke, B. (1986), Bidirectional reflectance spectroscopy: 4. The extinction coefficient and the opposition effect, *Icarus*, *67*(2), 264–280.
Hapke, B. (2002), Bidirectional reflectance spectroscopy: 5. The coherent backscatter opposition effect and anisotropic scattering, *Icarus*, *157*(2), 523–534, doi:10.1006/icar.2002.6853.
Hapke, B. (2008), Bidirectional reflectance spectroscopy: 6. Effects of porosity, *Icarus*, *195*(2), 918–926, doi:10.1016/j.icarus.2008.01.003.
Hapke, B., and E. Wells (1981), Bidirectional reflectance spectroscopy: 2. Experiments and observations, *J. Geophys. Res.*, *86*(B4), 3055–3060, doi:10.1029/JB086iB04p03055.
Hiroi, T., and C. M. Pieters (1994), Estimation of grain sizes and mixing ratios of fine powder mixtures of common geologic minerals, *J. Geophys. Res.*, *99*(E5), 10,867–10,879, doi:10.1029/94JE00841.
Klima, R. L., et al. (2011), New insights into lunar petrology: Distribution and composition of prominent low-Ca pyroxene exposures as observed by the Moon Mineralogy Mapper (M3), *J. Geophys. Res.*, *116*, E00G06, doi:10.1029/2010JE003719.
Kramers, H. A. (1927), La diffusion de la lumiere par les atomes, Atti del Congresso Internazionale dei Fisici, *Como*, *2*, 545–557.
Kreisch, C. D., J. A. O'Sullivan, R. E. Arvidson, D. V. Politte, L. He, N. T. Stein, J. Finkel, E. A. Guinness, M. J. Wolff, and M. G. A. Lapotre (2017), Regularization of Mars Reconnaissance Orbiter CRISM along-track oversampled hyperspectral imaging observations of Mars, *Icarus*, *282*, 136–151, doi:10.1016/j.icarus.2016.09.033.
Kronig, R. D. L. (1926), On the theory of dispersion of x-rays, *J. Opt. Soc. Am.*, *12*(6), 547–557.
Lapotre, M. G. A., B. L. Ehlmann, S. E. Minson, R. E. Arvidson, F. Ayoub, A. A. Fraeman, R. C. Ewing, and N. T. Bridges (2017), Compositional variations in sands of the Bagnold Dunes at Gale crater, Mars, from visible-shortwave infrared spectroscopy and comparison with ground truth from the Curiosity rover, *J. Geophys. Res. Planets*, doi:10.1002/2016JE005133.
Liu, Y., T. D. Glotch, N. A. Scudder, M. L. Kraner, T. Condus, R. E. Arvidson, E. A. Guinness, M. J. Wolff, and M. D. Smith (2016), End-member identification and spectral mixture analysis of CRISM hyperspectral data: A case study on southwest Melas Chasma, Mars, *J. Geophys. Res. Planets*, *121*, 2004–2036, doi:10.1002/2016JE005028.
Lucey, P. G. (1998), Model near-infrared optical constants of olivine and pyroxene as a function of iron content, *J. Geophys. Res.*, *103*(E1), 1703–1713, doi:10.1029/97JE03145.
McCord, T. B., et al. (1998), Salts on Europa's surface detected by Galileo's near infrared mapping spectrometer, *Science*, *280*(5367), 1242–1245.
McGuire, A. F., and B. W. Hapke (1995), An experimental study of light scattering by large, irregular particles, *Icarus*, *113*(1), 134–155.
Metropolis, N., A. W. Rosenbluth, M. N. Rosenbluth, A. H. Teller, and E. Teller (1953), Equation of state calculations by fast computing machines, *J. Chem. Phys.*, *21*(6), 1087–1092.
Minson, S. E., M. Simons, and J. Beck (2013), Bayesian inversion for finite fault earthquake source models I—Theory and algorithm, *Geophys. J. Int.*, *194*(3), 1701–1726, doi:10.1093/gji/ggt180.
Minson, S. E., M. Simons, J. Beck, F. Ortega, J. Jiang, S. Owen, A. Moore, A. Inbal, and A. Sladen (2014), Bayesian inversion for finite fault earthquake source models II—The 2011 great Tohoku-Oki, Japan earthquake, *Geophys. J. Int.*, *198*(2), 922–940, doi:10.1093/gji/ggu170.
Morris, R. V., D. C. Golden, J. F. Bell, H. V. Lauer, and J. B. Adams (1993), Pigmenting agents in Martian soils: Inferences from spectral, Mössbauer, and magnetic properties of nanophase and other iron oxides in Hawaiian palagonitic soil PN-9, *Geochim. Cosmochim. Acta*, *57*(19), 4597–4609.
Mustard, J. F., and C. M. Pieters (1987), Quantitative abundance estimates from bidirectional reflectance measurements, *J. Geophys. Res.*, *92*(B4), E617–E626, doi:10.1029/JB092iB04p0E617.
Mustard, J. F., and C. M. Pieters (1989), Photometric phase functions of common geologic minerals and applications to quantitative analysis of mineral mixture reflectance spectra, *J. Geophys. Res.*, *94*(B10), 13,619–13,634, doi:10.1029/JB094iB10p13619.
Nash, D., and J. Conel (1974), Spectral reflectance systematics for mixtures of powdered hypersthene, labradorite, and ilmenite, *J. Geophys. Res.*, *79*(11), 1615–1621, doi:10.1029/JB079i011p01615.
Pilorget, C., J. Fernando, B. L. Ehlmann, F. Schmidt, and T. Hiroi (2016), Wavelength dependence of scattering properties in the VIS–NIR and links with grain-scale physical and compositional properties, *Icarus*, *267*, 296–314, doi:10.1016/j.icarus.2015.12.029.
Poulet, F., and S. Erard (2004), Nonlinear spectral mixing: Quantitative analysis of laboratory mineral mixtures, *J. Geophys. Res.*, *109*, E02009, doi:10.1029/2003JE002179.
Poulet, F., J. Cuzzi, D. Cruikshank, T. Roush, and C. Dalle Ore (2002), Comparison between the Shkuratov and Hapke scattering theories for solid planetary surfaces: Application to the surface composition of two centaurs, *Icarus*, *160*(2), 313–324, doi:10.1006/icar.2002.6970.
Poulet, F., N. Mangold, D. Loizeau, J.-B. Bibring, Y. Langevin, J. Michalski, and B. Gondet (2008), Abundance of minerals in the phyllosilicate-rich units on Mars, *Astron. Astrophys.*, *487*(2), L41–L44, doi:10.1051/0004-6361:200810150.
Poulet, F., J. Carter, J. Bishop, D. Loizeau, and S. Murchie (2014), Mineral abundances at the final four Curiosity study sites and implications for their formation, *Icarus*, *231*, 65–76, doi:10.1016/j.icarus.2013.11.023.
Purcell, E. M., and C. R. Pennypacker (1973), Scattering and absorption of light by nonspherical dielectric grains, *Astrophys. J.*, *186*, 705–714.

Ramsey, M. S., and P. R. Christensen (1998), Mineral abundance determination: Quantitative deconvolution of thermal emission spectra, *J. Geophys. Res.*, *103*(B1), 577–596, doi:10.1029/97JB02784.

Robertson, K. M., R. E. Milliken, and S. Li (2016), Estimating mineral abundances of clay and gypsum mixtures using radiative transfer models applied to visible-near infrared reflectance spectra, *Icarus*, *277*, 171–186, doi:10.1016/j.icarus.2016.04.034.

Roush, T. L. (2003), Estimated optical constants of the Tagish Lake meteorite, *Meteorit. Planet. Sci.*, *38*(3), 419–426, doi:10.1111/j.1945-5100.2003.tb00277.x.

Roush, T., J. Pollack, F. Witteborn, J. Bregman, and J. Simpson (1990), Ice and minerals on Callisto: A reassessment of the reflectance spectra, *Icarus*, *86*(2), 355–382.

Shkuratov, Y., L. Starukhina, H. Hoffmann, and G. Arnold (1999), A model of spectral albedo of particulate surfaces: Implications for optical properties of the Moon, *Icarus*, *137*(2), 235–246.

Souchon, A. L., P. C. Pinet, S. D. Chevrel, Y. H. Daydou, D. Baratoux, K. Kurita, M. K. Shepard, and P. Helfenstein (2011), An experimental study of Hapke's modeling of natural granular surface samples, *Icarus*, *215*(1), 313–331, doi:10.1016/j.icarus.2011.06.023.

Sunshine, J. M., and C. M. Pieters (1998), Determining the composition of olivine from reflectance spectroscopy, *J. Geophys. Res.*, *103*(E6), 13,675–13,688, doi:10.1029/98JE01217.

Thomas, N., and J. Bandfield (2013), Identification of spectral endmembers in CRISM data using factor analysis and target transformation, paper presented at 44th Lunar and Planet. Sci. Conf., The Woodlands, Tex.

Tirsch, D., R. Jaumann, A. Pacifici, and F. Poulet (2011), Dark aeolian sediments in Martian craters: Composition and sources, *J. Geophys. Res.*, *116*, E03002, doi:10.1029/2009JE003562.

Tompkins, S., J. F. Mustard, C. M. Pieters, and D. W. Forsyth (1997), Optimization of endmembers for spectral mixture analysis, *Remote Sens. Environ.*, *59*(3), 472–489.

Zeidler, S., T. Posch, H. Mutschke, H. Richter, and O. Wehrhan (2011), Near-infrared absorption properties of oxygen-rich stardust analogs—The influence of coloring metal ions, *Astron. Astrophys.*, *526*, A68, doi:10.1051/0004-6361/201015219.